VALIDATION OF PLANT BUZZ OPERATIONAL DATA USING SERPENT-DYN3D SEQUENCE

A Thesis
Presented to
The Academic Faculty

by

Coral Hannah Kazaroff

In Partial Fulfillment
of the Requirements for the Degree
Masters of Science in
Nuclear and Radiological Engineering

Georgia Institute of Technology
December 2020

COPYRIGHT © 2020 BY CORAL HANNAH KAZAROFF

VALIDATION OF PLANT BUZZ OPERATIONAL DATA USING SERPENT-DYN3D SEQUENCE

Approved by:

Dr. Dan Kotlyar, Advisor
School of Mechanical Engineering
Georgia Institute of Technology

Dr. Anna Erickson
School of Mechanical Engineering
Georgia Institute of Technology

Dr. Bojan Petrovic
School of Mechanical Engineering
Georgia Institute of Technology

Dr. Michelle Guzzardo
Framatome Inc.

Date Approved: November 12, 2020

I would like to dedicate this thesis to my family, friends, professors, team-mates, and colleagues that made my time at Georgia Tech a truly remarkable experience.

ACKNOWLEDGEMENTS

This work was funded through the Nuclear Regulatory Commission project number 31310018M0020. The author would also like to thank Framatome, Inc. for providing the useful data and information that made this work possible.

CONTENTS

LIST OF FIGURES

LIST OF TABLES

LIST OF SYMBOLS AND ABBREVIATIONS

2D	Two-Dimensional
3D	Three-Dimensional
BP	Burnable Poison
BW	Boron Worth
CBC	Critical Boron Concentration
IFBA	Integrable Fuel Burnable Absorber
LEU	Low Enriched Uranium
LWR	Light Water Reactor
MC	Monte Carlo
MWt	Mega-Watt Thermal
PWR	Pressurized Water Reactor
SWU	Separative Work Unit
T/H	Thermal Hydraulic
^{235}U	Uranium-235
UO_2	Uranium Dioxide
WABA	Wet Annular Burnable Absorber

SUMMARY

There is a desire in the nuclear industry to improve the economics associated with the nuclear fuel cycle by moving to longer operational periods. One way to do this is to use high-assay low-enriched uranium in place of low enriched uranium to increase a plant's cycle length and subsequently availability factor.

Due to the complexity of reactors, comprehensive computational modeling and analysis must be complete before moving to experimental work and eventually new plant construction. Two common computational methods are Monte Carlo methods and nodal diffusion methods. Monte Carlo methods are well-established stochastic methods that are known to generate reliable results, while nodal methods typically have lower accuracy but save significantly on computational resources. Both methods can be combined in a two-step sequence to model core behavior during fuel irradiation, where the lattice code is the first step and provides few-group homogenized cross-section inputs, and the nodal diffusion solver is the second and provides the full core solution.

The primary objective of the current thesis is to validate this traditional two-step computational approach against given plant data and typical reactor parameters. Such a validation is necessary for the design and modeling of alternative high-assay low-enriched fuel cycles with longer operational periods. In this work, the Monte Carlo-based Serpent code is coupled to the nodal diffusion code, DYN3D. The established computational framework relies on in-house parsing tools developed within the Computational Reactor Engineering (CoRE) group to link Serpent and DYN3D.

The validation data, denoted as the BUZZ Benchmark, focused on five cycles, and the analysis itself focused on the three benchmarking cycles. The first step in modeling these cycles was to generate the various cross-section types in Serpent. These accounted for central fuel layers, blanket fuel layers, and reflector assemblies for a total of 49 variations due to different enrichments and burnable absorber rod combinations. An in-house Python-based interface, *gcwrite*, was used to read the cross sections generated by Serpent and write them into formats compatible with DYN3D input files.

An introductory part of this thesis concentrates on preliminary studies regarding the economic benefits of high-enriched cores, where the primary outcome goal is to increase the economic margins associated with the nuclear fuel cycle. In future research, the results obtained here are intended to be applied in conjunction with the developed Serpent-DYN3D computational sequence to further investigate the behavior of a higher-enriched core.

Special attention was devoted to code-to-code verification prior to benchmarking the validation data. The verification between Serpent and DYN3D included 2D fuel assembly burnup analysis, 3D fuel assembly with dependencies analysis, and finally 2D full core comparisons of a fresh and 3-batch core. Very good agreement was obtained for all of the examined models. It must be emphasized that the verification work also included sensitivity on few-group cross-section generation, *e.g.*, number of energy groups. The rest of this thesis focuses on benchmarking the equilibrium cycle. The implemented equilibrium search was successfully applied to reproduce the performance of the benchmarked cycle.

CHAPTER 1. INTRODUCTION

This thesis looks into benchmarking a coupled Monte Carlo nodal diffusion code sequence against given plant data for the purpose of its application to model new fuel cycles. The Serpent-DYN3D sequence is used to perform various analyses including sensitivity analysis on few-group cross-sections and burnup analysis with thermal hydraulics. Finally, the nodal diffusion code will be used to replicate an equilibrium cycle. The following sections will outline the background and motivation of this research, the objectives of it, and finally, its methodology.

1.1 Motivation

The motivation for this work stems from the desire within the nuclear industry to improve the economic efficiency of the nuclear fuel cycle by moving to longer operational periods. Such an increase in cycle length increases the availability factor and potentially decreases the fuel cycle cost. One way to achieve this is through the use of high-assay low-enriched (below 7% enriched) uranium (HALEU) in place of the low-enriched uranium (LEU) currently used by operational plants. Before introducing such a change, however, extensive modeling and analysis must be performed.

An established computational sequence for modeling the core behavior during the fuel cycle irradiation period involves the use of lattice codes followed by the use of a nodal diffusion core solver, which provides the neutronic, thermal-hydraulic, and time-dependent solution. Typically, a lattice code, e.g. CASMO, is used to generate few-group homogenized cross-sections for all operational conditions (e.g. temperatures, burnup,

xenon), which are then inputted into a nodal code, e.g. PARCS, which acts as the core simulator.

In this thesis, the Monte Carlo-based Serpent code is coupled with the nodal diffusion code, DYN3D, with the goal of validating the sequence for future modeling of higher enriched cores. While previous studies have been performed on 2D fuel assemblies and results have been extrapolated to predict full core trends, a 3D full core model remains a necessary stage in accurately demonstrating the potential benefits of higher enriched cores. The computational sequence investigated in this thesis validates such a model against known data and proves its utility for studies with unknown data. It sets the stage for modeling the full core behavior, as the final model would simply require inputs of the higher enriched cross sections and would be a verified method for investigating HALEU trends.

1.2 Objectives

The main objective of this thesis is to validate the computational sequence against plant data for future application to new fuel cycles. This was accomplished by:

- Initial code-to-code verification between 2D and then 3D fuel assemblies.
- Expansion into 2D full-core sensitivity studies on cross-sections with respect to number of energy groups.
- Generation of all core cross-sections accounting for central fuel layers, blanket fuel layers, and reflector assemblies for a total of 49 cross-section types due to varying enrichments and burnable absorber rod combinations.

- Application of the full sequence to an equilibrium search for reproduction of the performance of the benchmarked cycle.

1.3 Scope

The first part of this thesis concentrates on preliminary studies regarding the economic benefits of high-enriched cores and provides a background for the motivation behind the final outcome goals. The next portion of this work focuses on a thorough code-to-code verification process involving 2D burnup analysis, 3D assembly analysis with T/H dependencies, and 2D full-core sensitivity studies. This was necessary to ensure reliability of results during the equilibrium benchmarking stages. All Monte Carlo simulations in this work were done with Serpent and all nodal diffusion runs were done with DYN3D. The third and primary stage of this thesis focuses on benchmarking the equilibrium cycle. Here, the sequence was applied to perform full core analysis with cross-sections generated by the Monte Carlo code, Serpent, in advance. The conclusions of this section are related back to the preliminary economic studies to demonstrate future goals in increasing the economic margins associated with the nuclear fuel cycle and how the initial stages of such a shift can be done computationally.

1.4 Thesis Layout

Chapter 2 presents relevant background information regarding reactor physics concepts, computational methods, and various codes and supporting tools utilized. It also presents information pertaining to the background of fuel cycles and motivation for this research. Chapter 3 describes a preliminary fuel cycle economic study in order to convey the background and motivation behind this work. Chapter 4 details material and geometry

specifications as well as operating conditions of the chosen system. Chapter 5 provides a description of the initial code-to-code verification process performed on the fuel assemblies, as well as material and geometry specifications. The 2D full-core sensitivity analyses with respect to few-group cross-sectional energy dependence are described in chapter 6. The equilibrium and benchmarking cycles are the focus of Chapter 7, which contains the bulk of the work performed. Finally, Chapter 8 details the conclusions, missing information, and possible future work.

CHAPTER 2. CODES AND METHODS

This chapter presents an overview of the computational methods, codes, and their applications to this thesis. A background on transport and diffusion methods is given in sections 2.1 and 2.2. This is followed by the application of these methods to Monte Carlo and nodal diffusion codes in section 2.3. Section 2.4 describes the specific codes used in this work as well as other computational tools and packages. The final section introduces the methodology implemented in 2D fuel cycle studies using the nonlinear reactivity model to determine the fuel cycle benefits of a higher enriched core using 2D fuel assemblies.

2.1 Neutron Transport

The most fundamental concept of predicting the behavior of a nuclear reactor relies on the motion and distribution of neutrons within the core. By studying these interactions, the stability of the fission chain reaction can be inferred. To do so, we must introduce the theory of neutron transport.

The neutron transport equation is a mathematical balance between neutrons leaving the system and neutrons entering the system. It is defined by an integrodifferential particle distribution and is linear in angular neutron density, $n(\boldsymbol{r}, E, \widehat{\boldsymbol{\Omega}}, t)$. This depends on seven independent variables: three in space $\boldsymbol{r} = (x, y, z)$, one in energy E, two in angle $\widehat{\boldsymbol{\Omega}} = (\theta, \phi)$, and one in time t. The fundamental form is represented by Equation 2.1 [15]:

$$\frac{\partial n}{\partial t} + v\widehat{\boldsymbol{\Omega}} \cdot \boldsymbol{\nabla} n + v\Sigma_t n\left(\boldsymbol{r}, E, \widehat{\boldsymbol{\Omega}}, t\right) \tag{2.1}$$

$$= \int_{4\pi} d\hat{\boldsymbol{\Omega}}' \int_0^{\infty} dE' v' \Sigma_s\left(E' \to E, \hat{\boldsymbol{\Omega}}' \to \hat{\boldsymbol{\Omega}}\right) n\left(\boldsymbol{r}, E', \hat{\boldsymbol{\Omega}}', t\right) + s(\boldsymbol{r}, E, \hat{\boldsymbol{\Omega}}, t)$$

Here, the left side represents neutrons lost through leakage and collision, while the right side represents neutrons gained through streaming, collision, and independent sources.

While the transport equation is widely regarded as the most fundamental and exact model of neutron behavior, it is most commonly used in small-scale problems, e.g. 2D fuel assemblies. Application of deterministic transport codes is not widely used or well-established, although there are several coarse-based transport codes that show great promise, e.g. RATTLESNAKE [24] and COMET [25]. A more elegant approach comes from gas dynamics in the form of the diffusion approximation, where transport corrections can be implemented into boundary conditions of a far simpler equation.

2.2 Neutron Diffusion

The diffusion approximation is derived from gas dynamics in which the motion of particles in liquid and gaseous environments is modeled. The underlying idea is that particles tend to move from regions of higher to lower density. It relates the current $\boldsymbol{J}$ to the flux ϕ by the proportionality constant D, or the diffusion coefficient. The result of this can then be substituted into the neutron balance equation. If material homogeneity is assumed, the diffusion coefficient can be taken as invariant with space, and the grad operator can be replaced by the Laplacian for the following approximation [16]:

$$\frac{1}{v}\frac{\partial \phi}{\partial t} - D\nabla^2\phi + \Sigma_a \phi = s \tag{2.2}$$

The above equation is the most rudimentary form of the diffusion equation, in which the source *s* includes both the flux dependent fission source as well as any other external sources. In steady-state problems, or more precisely, slow varying problems, e.g. fuel cycle analysis, the time derivative is replaced by the multiplication factor, also known as the fission eigen value. On practical terms, though, the critical state at any given time point is obtained by adjusting the macroscopic absorption eigen value.

While the diffusion equation can be fairly rigorous to derive, it serves as a reliable model and is significantly easier to solve than the transport equation. It becomes less applicable under certain conditions, such as high absorbing media, system boundaries, sources, sinks, and locations with large flux gradients. However, the addition of transport corrections can further increase its accuracy in modeling neutronic behavior and make it a reliable tool in various reactor codes, particularly in cases of modeling 3D full cores.

2.3 Computational Methods

2.3.1 Monte Carlo

The Monte Carlo technique is a stochastic approach to solve arbitrary problems that cannot be easily solved deterministically. Systematic errors in deterministic methods arise from discretization of the phase space in energy, time, angle, and space, whereas Monte Carlo methods maintain continuity of these variables in the transport equation. To do so, a finite number of particle histories is simulated through a pseudo-random number generator and probability distributions are sampled for all histories with respect to scattering angles, track length distances between collisions, etc. Tabulated cross-sectional data is used to determine reaction types in different materials for each particle.

Errors in this methodology are statistical by nature, and accuracy can be increased by increasing the number of particle histories. However, errors typically decrease by $N^{\frac{1}{2}}$, where N is the number of particles, thus decreasing computational efficiency as complexity of the problem increases. Another example in which the additional computational resources required can become prohibitive is the inclusion of depletion analysis and thermal hydraulics. This typically requires iteratively updating various local parameters with each step, including nuclide concentrations, temperatures, and power, and subsequently increases the computational burden.

2.3.2 Nodal Diffusion

By contrast, nodal methods rely on division of the reactor into discrete spatial regions, typically assemblies divided into axial layers. Group constants are generated in a preceding step from a lattice code and serve as inputs. These cross-sections are then used to solve the diffusion equation in each node and obtain a set of averaged values such as nodal-averaged flux. The nodal methodology is particularly favorable over fine-mesh transport in complex problems, where it becomes computationally expensive, for example, in cases of burnup analysis of a full core. One limitation in nodal diffusion methods is the problem of adjacent nodes with significantly different material properties where homogeneous and heterogeneous fluxes can vary greatly. However, these are accounted for in the lattice code-generated group constants as correction factors. Overall, nodal diffusion codes provide the ability to generate quicker solutions with less computational resources for the same problem in a lattice code but do require a preceding step reliant on a lattice code.

2.4 Codes

2.4.1 Serpent

The Monte Carlo code used in this work was Serpent. Serpent is a multipurpose 3D continuous energy Monte Carlo particle transport code developed at the VTT Technical Research Centre of Finland [2]. Serpent allows for the modeling of complex 3D geometries and can be used in fuel cycle analysis given its burnup capabilities. It was originally developed mainly as a tool for generation of homogenized few-group constants. This code allows for generation of cross sections for zero-leakage infinite lattices (INF) and for systems with non-zero leakage currents in which spectrum correction schemes (B1) are applied [3]. Serpent is continuously being updated and is now very attractive for multi-physics calculations, particularly for its efficient Woodcock Delta-tracking routine, which is faster in complex geometries and makes complicated objects and surfaces easier to handle [4]. In this thesis, Serpent 2 is used with the ENDF/B-VII [18] cross section library as a few-group constant generator for homogenized macroscopic and microscopic cross-sections, as well as for reference solutions for the cases analyzed.

2.4.2 DYN3D

The nodal diffusion code used in this work is DYN3D, a 3-dimensional nodal reactor dynamics code developed by the Helmholtz-Zentrum Dresden-Rossendorf in Germany [5]. It was mainly developed for analysis of transient scenarios in LWRs with square or hexagonal lattices, but its functionality has been expanded for steady-state and fuel cycle calculations, including decay heat calculations [17], as well as for triangular fuel assembly geometries [6]. Additionally, DYN3D has been shown to be a capable tool for

the modeling of Sodium Fast Reactors (SFRs) for reactors with oxide fuel [7]. Although DYN3D can be coupled with a number of system codes, as well as thermal hydraulic and fuel performance codes in order to expand its applicability, the work presented here relies only on neutronic analysis and thus no coupling of DYN3D with other codes was realized. In order to be executed, DYN3D needs to be provided with a pre-generated cross-section library. In this work, cross-section generation is done using the previously Monte Carlo code Serpent 2.

2.4.3 Other Tools

Various supporting tools were used both for pre-processing inputs and post-processing outputs. Isotope fraction calculations were automated in Matlab to ensure consistency in Serpent inputs for cross-section generation. Excel spreadsheets with shuffling keys were used in conjunction with Python scripts to shuffle the burnup distribution for each cycle based on the DYN3D output files. Finally, two in-house packages, *serpentTools* and *gcwrite*, were used together to parse Serpent outputs.

The serpent-tools Python package is a collection of parsing tools and containers aimed at expediting the analysis of Serpent outputs. Files that would make Matlab extremely slow or unresponsive can be processed within fractions of seconds, with no loss of data. The data is stored in an object-oriented framework that mimics the physical nature of the quantities represented, e.g. detector objects have tallies and grid structures, depleted material objects have names and associated atomic density, toxicity, and burnup matrices. Many of the readers and containers have routines for expediting common analyses, with heavy emphasis on plotting. Plots of cartesian and hexagonal detector meshes, flux spectra,

homogenized group constants, and depletion parameters are made accessible to the user, without requiring a steep learning curve. The project is hosted on GitHub with a permissive MIT license and is undergoing constant development and improvement. A thorough overview of the supported file types with corresponding examples can be found throughout the repository [8].

Gcwrite is another Python package that also employs serpent-tools and writes the Monte Carlo output cross-sections into files that are compatible with required DYN3D input formats.

2.5 2D Fuel Cycle Analysis

Preliminary fuel cycle calculations were performed on 2D fuel assemblies to estimate the potential benefits of a shift to the 24-month cycle length. Core performance was evaluated using a 2D assembly setup in conjunction with the non-linear reactivity model. A calculation sequence was developed in three major parts involving estimation of critical boron concentration, evaluation of burnable designs and varying enrichment levels, and economic analysis. The following sections present the methodology as well as models used to perform these analyses.

2.5.1 Estimation of Core CBC

An established means of PWR reactivity control is the dissolution of boron in the reactor coolant. The maximum concentration of soluble boron is limited primarily by the coolant chemistry considerations to about 2,000 ppm, but also by the coolant temperature reactivity coefficient. In this preliminary study, the upper limit of the boron concentration

was set to 1,500 ppm at xenon equilibrium. The following methodology was used to estimate core CBC based on assembly-level calculation data.

1. Perform a fuel assembly burnup calculation with zero boron concentration.
2. Fit the calculated fuel assembly reactivity (ρ) vs. burnup (BU) data to a 3rd order polynomial function as described in Equation 2.3:

$$\rho(BU) = a_0 + a_1 BU + \cdots + a_3 BU^3 \tag{2.3}$$

3. At each burnup point, use the built-in restart option in Serpent to alter the boron concentration (ppm) and obtain the boron worth (BW) as a function of burnup:

$$BW(BU) = \frac{\Delta\rho(BU)}{\Delta ppm} = \frac{\rho(BU, ppm_2) - \rho(BU, ppm_1)}{ppm_2 - ppm_1} \tag{2.4}$$

where *BW(BU)* is the assembly soluble boron worth defined as the reactivity change per unit ppm change in the soluble boron concentration.

4. From the results obtained in the previous step, a fit can be derived for assembly BW vs. burnup data for a 2nd order polynomial, as show in Equation 2.5:

$$BW(BU) = c_0 + c_1 BU + c_2 BU^2 \tag{2.5}$$

5. Next, the core reactivity was obtained using:

$$\rho_{core}(BU) = \frac{1}{N}\sum_{i=0}^{N-1} N_i \rho\left(BU + iB_{cycle}\right) - \rho_L \tag{2.6}$$

where N_i is the number of fuel assemblies for batch i and $N = \sum N_i$. Assuming the power share among the fuel batches is equal, B_{cycle} can be calculated using the following relation:

$$\frac{1}{N}\sum_{i=1}^{N} N_i \rho\left(iB_{cycle}\right) = \rho_L \tag{2.7}$$

This allows for core reactivity as a function of burnup to be determined using a single assembly and cycle burnup. This approach is consistent with the non-linear reactivity model, where core reactivity is assumed to be an average of individual assemblies [12].

7. Since *BW* varies with burnup, different fuel batches will have different *BW* at each burnup point. The core *BW* as a function of burnup can be obtained in a similar manner to $\rho_{core}(BU)$, as shown in Equation 2.8:

$$BW_{core}(BU) = \frac{1}{N}\sum_{i=0}^{N-1} N_i \cdot BW(BU + iB_{cycle}) \tag{2.8}$$

8. After obtaining the core reactivity as a function of burnup, an expression for the CBC can be developed:

$$CBC(BU) = \frac{\rho_{core}(BU)}{BW_{core}(BU)} \tag{2.9}$$

The number of burnable poison pins and the Gd_2O_3 concentration (homogeneously mixed with the UO_2) were adjusted to satisfy the upper CBC limit of 1,500 ppm. This properly accounts for any residual reactivity penalty due to the incomplete burnup of BP material.

2.5.2 Economic Evaluation Models

This section presents the methodology adopted for evaluating the results of the assembly study and comparing fuel cycle costs for 18- versus 24-month cycle lengths. A simplified economic model was used in which inflation was disregarded. The model relied on the cost of U_3O_8 per kg, conversion cost of UF_6 per kg, and the Separative Work Unit (SWU). The SWU values were assumed to be linear up to 6.5 w/o. The values were

obtained from the Ux Consulting Company website and are based on the Month-End prices of March 2019 [14]. See Table 2-1 for prices.

Table 2-1 UxC spot prices for uranium, conversion, and SWU

Symbol	Product	Price, $
P_U	U_3O_8, kg	56.8
P_C	Conversion price, kgU	14.75
P_S	SWU price	43.00
P_F	Fabrication costs, kgU	400.00

The separation potential functions V(x_i) for product ($x_p = 0.045/0.065$), waste ($x_w = 0.0020$), and feed ($x_f = 0.00711$) were calculated by Equation 2.10:

$$V(x_i) = (2x_i - 1)\ln\left(\frac{x_i}{1 - x_i}\right) \tag{2.10}$$

The feed factor (FF) and the waste factor (WF) were evaluated using Equation 2.11:

$$FF = \frac{F}{P} = \frac{x_p - x_w}{x_f - x_w}$$
$$WF = \frac{W}{P} = FF - 1 \tag{2.11}$$

The separation potential functions, the feed factor, and the waste factor were then used to calculate the SWU factor (S), which describes the number of SWUs required per enriched kgU:

$$S = \frac{SWU}{P} = V(x_p) + WF \times V(x_w) - FF \times V(x_f) \tag{2.12}$$

The conversion and fabrication losses were neglected and the price (P_E) of enriched uranium was calculated using the following relation:

$$P_E = (P_U + P_C \times f_s) \times FF + P_S \times S \tag{2.13}$$

The total cost (P_T) of the fuel per kg-U was calculated by adding the fabrication costs (P_F) to the enrichment costs:

$$P_T = P_E + P_F \tag{2.14}$$

To estimate the fuel costs and outage costs, in terms of ¢/kWhe, the cycle length (T_C) and discharge burnup (B_d) with the thermal to electric conversion efficiency (η) of 34% were used as described in Equation 2.15:

$$Fuel\ costs = \frac{P_T}{B_d \times \eta}\left[\frac{¢}{\mathrm{kWh_e}}\right]$$

$$Outage\ costs = \frac{Total\ cost\ of\ outage}{Power \times T_c \times \eta}\left[\frac{¢}{\mathrm{kWh_e}}\right] \tag{2.15}$$

CHAPTER 3. FUEL CYCLE STUDY

This chapter seeks to further convey the motivation behind this work as well as outline the economic considerations associated with the nuclear fuel cycle by presenting the results of a study performed on 2D fuel assemblies and extrapolating the economic benefits of higher enriched assays to a full core model.

3.1 Overview

There is motivation within the nuclear industry to move to longer operational periods. Such an increase in cycle length increases the availability factor of a power plant, potentially decreasing the fuel cycle costs. The strong correlation between cycle length and enrichment suggests one way of doing so is to increase the average uranium enrichment within the core. However, NRC regulations on uranium enrichment limit the maximum nominal ^{235}U enrichment of the fresh fuel assemblies to 5% by weight [9]. While several facilities retain the ability to produce fuel for HALEU reactors, these facilities are not capable of supplying fuel to the current LWR fleet [10]. If the benefits of higher enriched fuel can be demonstrated, a licensed approval for specific plant usage would be the next step needed.

Before any of this, however, it must be theoretically proven that increasing uranium enrichment and burnup limits would pose non-negligible economic benefits to the fuel cycle. In particular, it must be thoroughly shown that a model of a higher-enriched core is both safe and feasible. The analyses of this thesis seek to begin proving so. By validating

the code sequence and modeling given data, it intends to show that such a sequence can be used to model a new, higher-enriched core in the future.

In this study, fuel cycle analysis was performed on 2D fuel assemblies for chosen enrichments and numbers of burnable poison pins. The nonlinear reactivity model was then applied to evaluate core performance depending on 2D fuel assembly performance. Various configurations were analyzed with the purpose of obtaining the enrichment value for a desired cycle length of 24 months. Only then the economics could be analyzed.

3.2 Enrichment Study Results

In order to determine the fissile loading required to achieve certain cycle lengths, a series of fuel assembly calculations was performed. The ^{235}U weight enrichment in the fuel was varied between 4.0 and 6.7 percent by weight. Figure 3-1 presents the reactivity curves of these calculations which were then used to calculate core reactivity using the methodology discussed in the previous chapter.

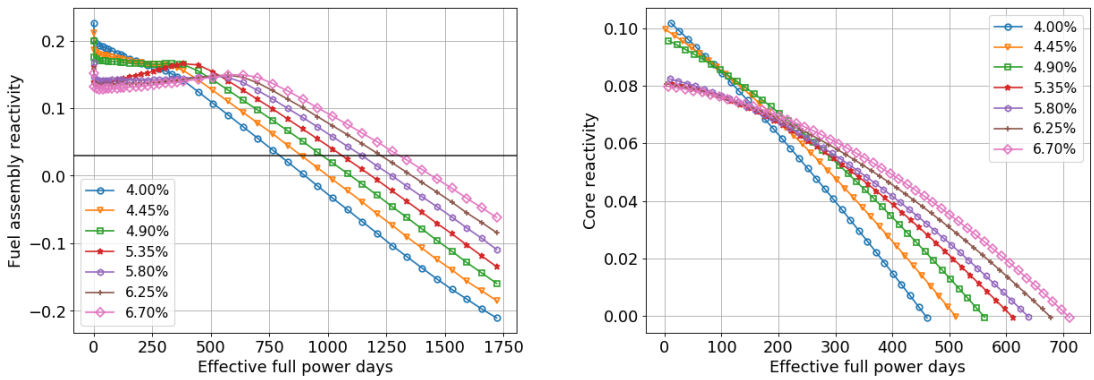

Figure 3-1 Assembly and core reactivity for varying uranium enrichments

Increasing the ^{235}U content in the assemblies results in higher excess reactivity, which must be controlled with burnable poisons and soluble boron. As shown above in Figure 3-1, the maximum core reactivity obtained by each of the configurations is higher for lower enrichment values and considerably lower for higher enrichment values.

Another noteworthy observation is that increasing the ^{235}U enrichment consistently decreases the negative boron worth. This is due to hardening of the spectrum in the presence of more ^{235}U. Therefore, an increased amount of soluble boron is required to maintain core criticality.

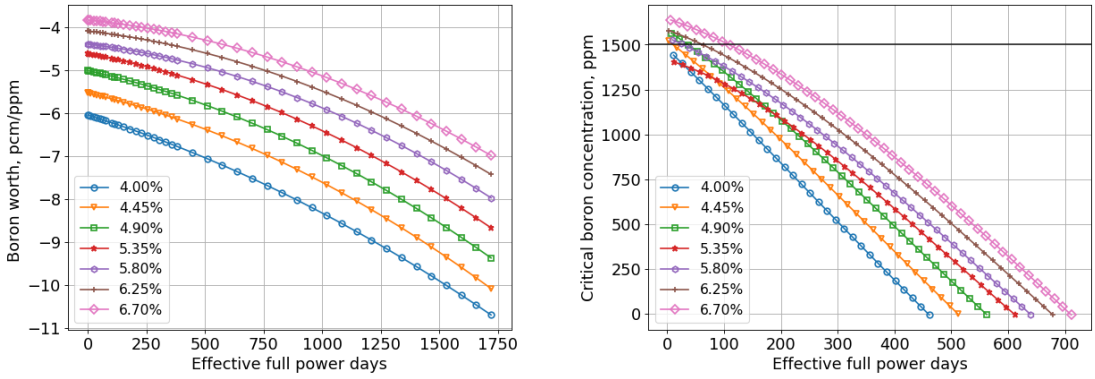

Figure 3-2 (L) BW for varying enrichments (R) CBC for varying enrichments

Figure 3-3 demonstrates that increasing the ^{235}U enrichment and adding additional BP pins leads to a nonlinear increase in cycle length. The marginal cycle length gains are reduced as the enrichment and number of BP pins grows. The correlation of the cycle length against enrichment, as shown in Figure 3-3, yields a convex quadratic curve, reinforcing this claim. Applying a quadratic fit, the enrichments required for 18- and 24-month cycles were found to be 4.27 and 6.13 w/o ^{235}U, respectively.

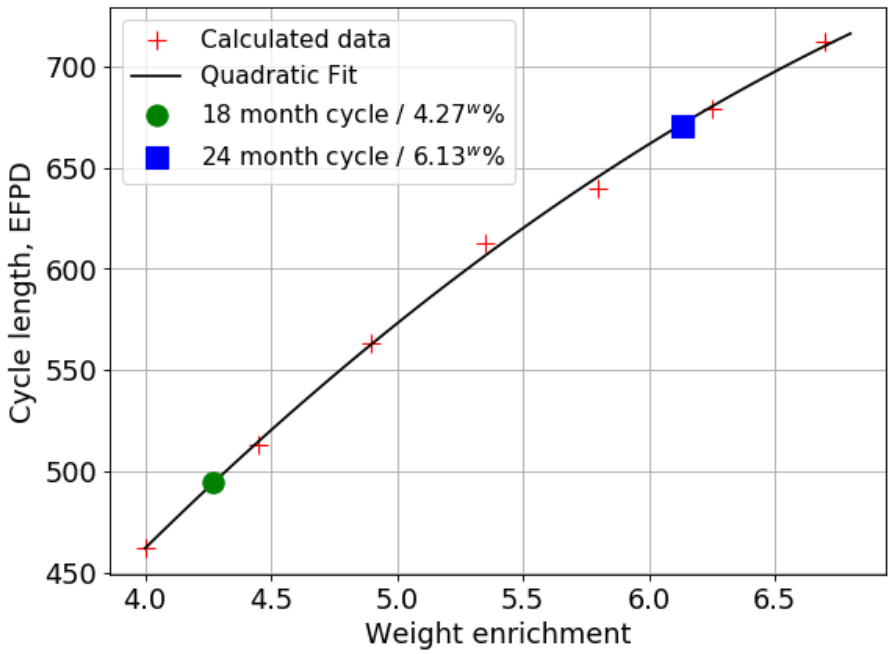

Figure 3-3 Quadratic fit of cycle length as a function of weight percent enrichment of uranium

The results of the fuel assembly analysis provide a starting point for analyzing the economics associated with higher enriched cycles. A comparison of the two identified enrichments of 4.27 and 6.13 w/o ^{235}U using the methodology described in Chapter 2 demonstrate the significance of shifting to 24-month cycles as well as motivation for future studies implementing full-core analysis and thus requiring verification of a full-core sequence.

3.3 Economic Analysis

For the economic analysis, a simplified model was used in which inflation was ignored. Natural enrichment was taken to be 0.711% and tail enrichment to be 0.20%. Stepwise values for each enrichment were combined with cost data to determine the cost

at each stage of the fuel cycle as well as a final total cost per kgU. These values are presented in Table 3-1.

Table 3-1 UxC spot prices for uranium, conversion, and SWU

Process	4.27 w/o ^{235}U		6.13 w/o ^{235}U	
	Required	Cost	Required	Cost
U_3O_8, kg	8.0 kg	451.8	11.6 kg	659.0
Conversion	8.0 kg	117.4	11.6 kg	171.2
Enrichment	7.2 SWU	307.6	11.5 SWU	495.2
Fabrication		400.0		400.0
Total, $		1,276.9		1.725.5

Calculated costs for each enrichment were combined with efficiency and discharge burnup to determine fuel costs from Equation 2.15. In order to calculate the outage cost per kWhe, the total outage cost was assumed to be $30 million. The fuel and outage costs can be added together to find the cumulative cost in terms of cents/kWhe.

Table 3-2 Fuel cycle costs [$] for 1 kg of uranium

Parameter	**4.27 wt%**	**6.13 wt%**
Cycle length	18 mo.	24 mo.
Assembly/pin B_d, MWd/MTU	46,800/56,200	63,500/76,100
Fuel cost, cents/kWhe	0.334	0.333
Outage, cents/kWhe	0.204	0.150
Total, cents/kWhe	0.538	0.484 (-10%)

The conclusions reached in this economic analysis confirm the benefits of pursuing longer cycle lengths and indicate that 10% fuel cost savings are attainable. They subsequently provide motivation for the remainder of the work done in this thesis, as it is necessary to expand from 2D fuel assembly calculations to 3D full core analysis. The

validation of the code sequence that is the focus of this thesis sets future work up to model the full core with the fuel enriched to the higher value of 6.13%. Such work intends to provide conclusive evidence and motivation to look into current regulations in the hope of further optimizing the nuclear fuel cycle.

CHAPTER 4. MODEL DESCRIPTION

4.1 Overview

This chapter will provide an overview of the geometry and material descriptions of the system used as well as its operational parameters. The reactor under consideration is a standard 4-loop Westinghouse PWR operating at 3600 MW_{th} [1]. The geometry and materials are presented in increasing levels of hierarchy including pin, assembly, and full core.

4.2 Geometry and Material Descriptions

The core geometry specifications are described in three hierarchical levels, each detailed in increasing scope. The lowest level begins with the radial geometry of each pincell type used in the core. The fuel assemblies are subsequently described, with each possible configuration included to demonstrate the ways to include two types of burnable absorber rods. The geometry description is followed by material specifications. Each table lists the component isotopes for each material accompanied by either atomic or weight fraction.

4.2.1 Pin Geometry

In this section, the radial parameters of each pincell type used in the fuel assemblies are detailed. Each describes a complete pincell surrounded by the primary coolant. There are five types of pins, including bare fuel pins, fuel pins with an integrable fuel burnable absorber (IFBA), wet annular burnable absorber (WABA), and guide/instrument tubes.

The instrument tubes take the place of the central rod in each fuel assembly, while each assembly contains 24 guide tubes that can be replaced by up to 24 WABA rods. For all of the figures, materials and dimensions are detailed in order from the inner region to the outer region.

Fuel Pin

Region	Radius (cm)	Material
1	0.392176	Fuel
2	0.400050	Helium
3	0.457200	Clad

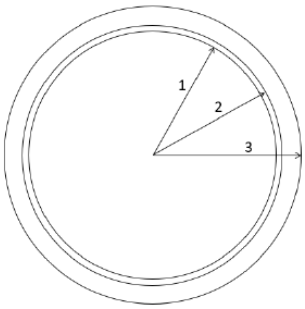

Figure 4-1 Fuel pin radial geometry configuration

IFBA Pin

Region	Radius (cm)	Material
1	0.196850	Void
2	0.392176	Fuel
3	0.393176	ZrB_2
4	0.400050	Helium
5	0.457200	Clad

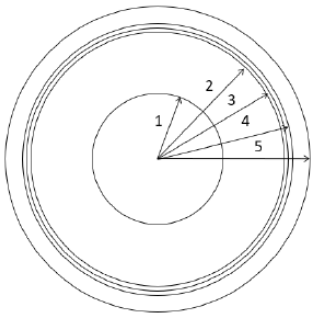

Figure 4-2 IFBA pin radial geometry configuration

WABA Pin

Region	Radius (cm)	Material
1	0.29000	Void
2	0.34000	Inner clad
3	0.35000	Void
4	0.40386	Al_2O_3-B_4C
5	0.41783	Void
6	0.48387	Outer clad

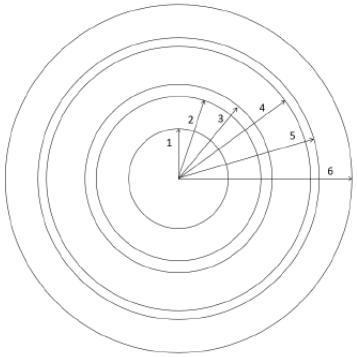

Figure 4-3 WABA pin radial geometry configuration

Instrument/Guide Tube

Region	Radius (cm)	Material
1	0.56134	Void
2	0.61214	Zirc4

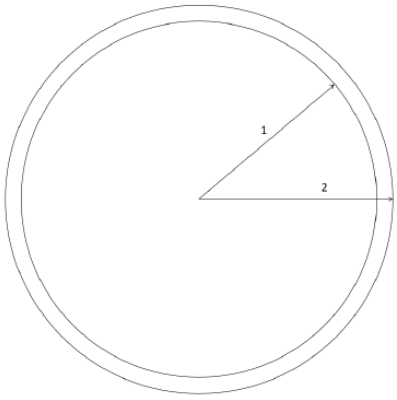

Figure 4-4 Instrument/guide tube radial geometry configuration

4.2.2 Fuel Assembly Configurations

Each of the core assemblies is composed of a 17x17 array of pins. Table 4-1 outlines the important assembly parameters, and the various configurations are shown below. The assemblies are made of one of four different fuel enrichment pins and guide tube positions

can be filled with either guide tubes or WABA rods. Up to 156 of the fuel pin positions can be replaced with IFBA rods, and the central location in each assembly is reserved for an instrumentation tube.

Table 4-1 Fuel Assembly Parameters

No. Fuel Rods	264
No. Guide Tube Positions	24
No. Instrument Guide Tubes	1
Fuel Assembly Lattice Pitch	21.50364 cm
Pin Lattice Pitch	1.259840 cm
Pin Lattice Configuration	17x17

There are various assembly configurations with respect to uranium enrichment and number of burnable absorber rods; these rely both on IFBA and WABA. Figure 4-5 demonstrates all the possible IFBA configurations, Figure 4-6 demonstrates the possible WABA configurations, and Figure 4-7 shows only a sample of possible combinations of the two. Pink color denotes the normal UO_2 fuel pins, green color denotes IFBA rods, yellow color represents WABA rods, white color is the central instrument tube, blue color denotes guide tubes, and the surrounding blue color is used to represent the water moderator.

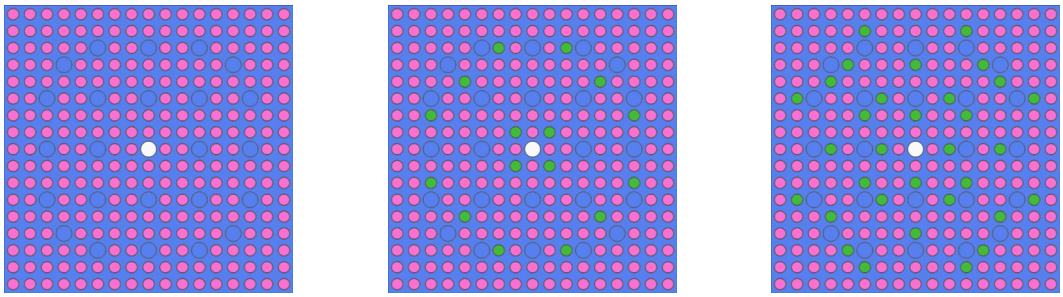

(a) 0 IFBA (b) 16 IFBA (c) 32 IFBA

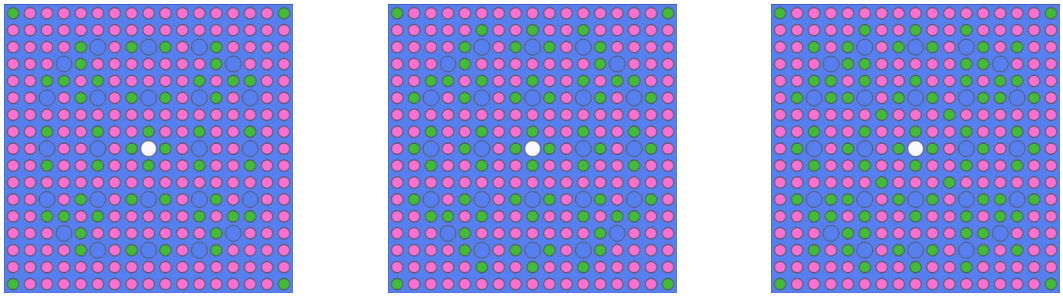

(d) 48 IFBA (e) 64 IFBA (f) 80 IFBA

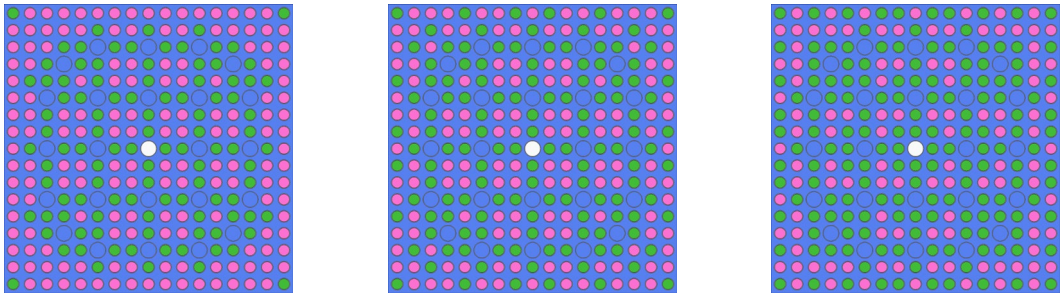

(g) 104 IFBA (h) 128 IFBA (i) 156 IFBA

Figure 4-5 All configurations of IFBA rods with no WABA rods; fuel and IFBA pins are denoted by the pink and green color, respectively

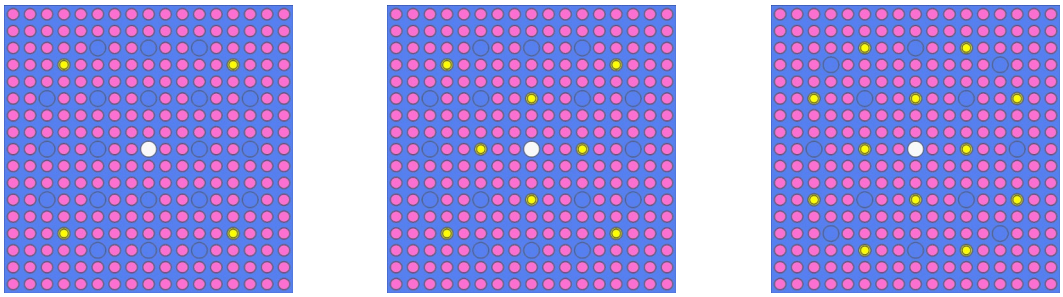

(a) 4 WABA (b) 8 WABA (c) 12 WABA

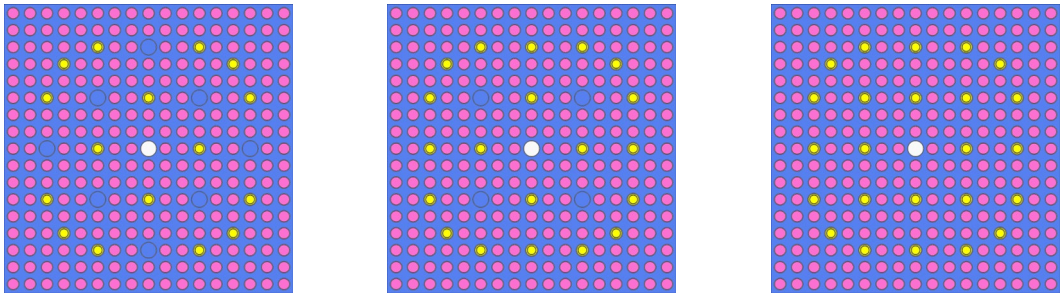

(d) 16 WABA (e) 20 WABA (f) 24 WABA

Figure 4-6 All configurations of WABA rods with no IFBA rods; fuel and WABA pins are denoted by the red and yellow color, respectively

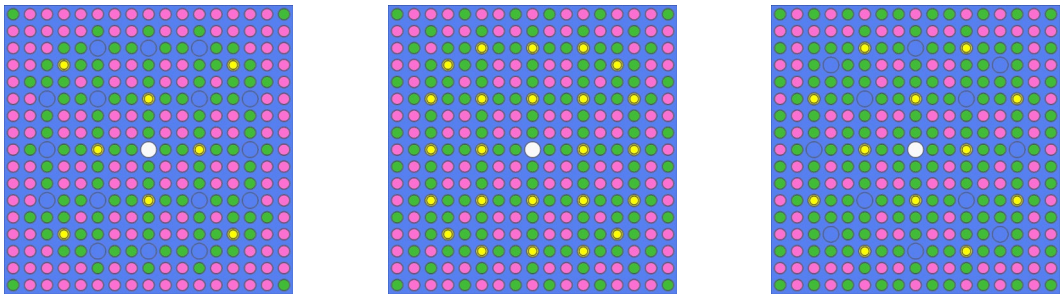

(a) 104 IFBA, 8 WABA (b) 128 IFBA, 24 WABA (c) 156 IFBA, 12 WABA

Figure 4-7 Example of IFBA/WABA configurations

4.2.3 Material Description

This section presents the various materials used in the design. There were four different fuel enrichments used in UO_2 pins and IFBA pins, varying between 4.0% and 4.95%.

Table 4-2 Material compositions for various UO_2 fuel enrichments

Fuel 4.0% Enriched	
Density (g/cc)	10.2141
Isotope	Mass Fraction
U-234	0.0002821423
U-235	0.0352677900
U-238	0.8461448000
O-16	0.1180178000
O-17	0.0002874819

Fuel 4.4% Enriched	
Density (g/cc)	10.2557
Isotope	Mass Fraction
U-234	0.0003103546
U-235	0.038794330
U-238	0.842584600
O-16	0.118023200
O-17	0.000287495

Fuel 4.6% Enriched	
Density (g/cc)	10.2558
Isotope	Mass Fraction
U-234	0.0003244607
U-235	0.0405575800
U-238	0.8408046000
O-16	0.1180259000
O-17	0.0002875016

Fuel 4.95% Enriched	
Density (g/cc)	10.3391
Isotope	Mass Fraction
U-234	0.000349146
U-235	0.043643250
U-238	0.837689500
O-16	0.118030600
O-17	0.000287513

The material coating used in the WABA pins is a mix of Al_2O_3 and B_4C enriched to 14 w/o ^{10}B. Similarly, the IFBA pin coating is composed of ZrB_2, assumed to be natural zirconium mixed with the ^{10}B poison.

Table 4-3 Material compositions for burnable absorber coatings

Al_2O_3-B_4C Annular WABA Pellets	
B_4C (14 w/o)	
Density (g/cc)	2.52
Isotope	Atomic Density (atom/b-cm)
C-12	7.10787570e-04
B-10	2.84315028e-03
Al_2O_3 (86 w/o)	
Density (g/cc)	3.95
Isotope	Atomic Fraction
Al-27	0.4
O-16	0.6

ZrB_2 IFBA coating	
Density (g/cc)	6.085
Isotope	Atomic Density (atom/b-cm)
Nat. Zr	1.06265294e-02
B-10	2.12530588e-02

The following materials make up the pin gaps, structural material, coolant, and cladding.

Table 4-4 Material compositions for gaps and coolant

Air	
Density (g/cc)	0.000616
Isotope	Atomic Density (atom/b-cm)
Ar-36	7.87290e-10
Ar-38	1.48440e-10
Ar-40	2.35060e-07
C-12	6.75640e-09
N-14	1.96810e-05
N-15	7.18990e-08
O-16	2.01370e-09
O-17	5.28630e-06

Helium	
Density (g/cc)	0.0015981
Isotope	Atomic Density (atom/b-cm)
He-3	3.22190e-10
He-4	2.40440e-04

Water	
Density (g/cc)	0.701468
Isotope	Mass Fraction (atom/b-cm)
B-10	2.690926e-04
B-11	0.0011909074
H-1	0.1117349725
O-16	0.8868050275

Table 4-5 Material compositions for stainless steel and zircaloy clad

Stainless Steel 304

Density (g/cc)			8.03
Isotope	Atomic Density (atom/b-cm)	Isotope	Atomic Density (atom/b-cm)
Si-28	9.52760e-04	Fe-56	5.43450e-02
Si-29	4.84010e-05	Fe-57	1.23310e-03
Si-30	3.19440e-05	Fe-58	1.67030e-04
Cr-50	7.67780e-03	Ni-58	5.60890e-03
Cr-52	1.48060e-02	Ni-60	2.16050e-03
Cr-53	1.67890e-03	Ni-61	9.39170e-05
Cr-54	4.17910e-04	Ni-62	2.99460e-04
Mn-55	1.76040e-03	Ni-64	7.62520e-05
Fe-54	3.46200e-03		

Zircaloy 4

Density (g/cc)			6.55
Isotope	Atomic Density (atom/b-cm)	Isotope	Atomic Density (atom/b-cm)
Cr-50	3.29620e-06	Sn-112	4.67350e-06
Cr-52	6.35640e-06	Sn-114	3.17990e-06
Cr-53	7.20760e-06	Sn-115	1.63810e-06
Cr-54	1.79410e-06	Sn-116	7.00550e-05
Fe-54	8.66990e-06	Sn-117	3.70030e-05
Fe-56	1.36100e-04	Sn-118	1.16690e-04
Fe-57	3.14310e-06	Sn-119	4.13870e-05
Fe-58	4.18290e-07	Sn-120	1.56970e-04
Zr-90	2.18270e-02	Sn-122	2.23080e+00
Zr-91	4.76000e-03	Sn-124	2.78970e-05
Zr-92	7.27580e-03	O-16	3.07430e-04
Zr-94	7.37340e-03	O-17	1.17110e-07
Zr-96	1.18790e-03		

The following material was used to model the reflectors on the core periphery. In the Serpent model, a homogeneous lattice was created using such material and placed adjacent to the edge fuel assemblies. To achieve the same results in DYN3D, a supercell was first created in Serpent with reflector material surrounded by a model fuel assembly and cross-sections were generated for the central reflector universe. This cross-section type was used as a periphery assembly in DYN3D in a similar manner to the Serpent reflectors.

Table 4-6 Material composition for reflector

Reflector			
Density (atomic)			0.070462
Isotope	Atomic Density (atom/b-cm)	Isotope	Atomic Density (atom/b-cm)
Zr-90	5.9311e-03	Cr-53	5.3951e-03
Zr-91	1.2934e-03	Cr-54	1.3430e-03
Zr-92	1.9770e-03	Ni-58	1.7122e-02
Zr-94	2.0035e-03	Ni-60	6.5978e-03
Zr-96	3.2278e-04	Ni-61	2.8421e-04
Fe-54	1.1217e-02	Ni-62	9.1398e-04
Fe-56	1.7738e-01	Ni-64	2.3290e-04
Fe-57	4.2545e-03	Mn-55	5.6687e-03
Fe-58	5.4149e-04	H-1	4.7165e-01
Cr-50	2.4673e-03	O-16	2.3583e-01
Cr-52	4.7580e-02		

4.3 Description of Core Parameters

The core under consideration is composed of 193 fuel assemblies and 64 reflector assemblies for a total of 257. Certain pin types within the assemblies vary axially as seen in Figure 4-8, which presents the fuel geometry based on axial height.

Axial Height, in	Segment Height, in	Axial Zones	WABA BPRA	UO2+IFBA Fuel Rod	UO2 Fuel Rod
138 – 144	6	Top Axial Zone	6" 0.0 BP (Cutback Region)	6" Annular Pellet, Central Enrichment	144" Solid Pellet, Central Enrichment
6 – 138	132	Central Zone, UO2 or UO2+IFBA and/or WABA BPRA Insert	132" centered BPRA Insert Al2O3-B4C Annular Pellet	132" Solid Pellet, Central Enrichment, ZrB2 Coating	
0 – 6	6	Bottom Axial Zone	6" No BP (Nothing)	6" Annular Pellet, Central Enrichment	

Figure 4-8 Axial geometry of Buzz Unit 1 fuel

Table 4-7 presents a detailed description of the operating parameters. Nominal power is 3626 MW_{th}, or a power density of around 44 W/g depending on the specific cycle. Constant coolant, fuel, and other material temperatures were used for simplicity throughout the benchmark.

Table 4-7 Buzz Unit 1 cycle parameters

Cycle	**45**	**46**	**47**
Duration (days)	516	506	535
EOC BU (MWd/kgU)	22.6581	21.84	23
Feed batch size	93	85	92
Rated power (MW)	3626	3626	3626

Pressure (bar)	155.14	155.14	155.14
Flowrate (Mlbm/hr)	132.5626	132.5626	132.5626
Core loading (MtU)	81.5005	81.4931	81.3867
Assembly loading (mtU)	422.282	422.485	421.693
Power density (W/g)	44.491	44.495	44.553
Cycle	**48**	**49**	**50**
Duration (days)	520	531	---
EOC BU (MWd/kgU)	22.7604	22.4704	---
Feed batch size	88	89	88
Rated power (MW)	3626	3626	3626
Pressure (bar)	155.14	155.14	155.14
Flowrate (Mlbm/hr)	132.5626	132.5626	132.5626
Core loading (MtU)	81.3842	81.325	81.2533
Assembly loading (mtU)	421.68	421.373	421.002
Power density (W/g)	44.554	44.587	44.626

CHAPTER 5. SERPENT-DYN3D VERIFICATION

5.1 Cross-Section Generation

DYN3D is a nodal diffusion code and thus requires spatial subdivision of the model into nodes. For the 3D fuel assembly, the model was axially divided into 24 nodes, where each node was given a separate set of input cross-sections based on its material type – central fuel, blanket fuel, or reflector. Each of these input cross-section types is a homogeneous representation of the materials in that region, and the associated input file contains the following various parameters:

- Transport cross-section
- Reduced absorption cross-section
- Nu-fission cross-section
- Kappa-fission cross-section
- Scattering cross-section matrices
- Assembly discontinuity factors
- Fission spectrum
- Inverse velocity

Where all but delayed neutron decay constant (lambda) and delayed neutron fraction (beta) are energy group dependent. Group constants are generated for each burnup step and each T/H perturbation in the case involving them.

The generation of cross-sections in the lattice code is a necessary and important preceding stage of performing the 3D fuel assembly and eventually full-core analyses in DYN3D. The fidelity of the coupled results is largely dependent on the group constants used. In this work, a 2-group energy structure was used with B1 leakage-corrected cross sections. Various sensitivities were performed to determine this group structure and will be discussed in the following chapter, as this current chapter merely seeks to demonstrate agreement between cases for the two codes.

5.1.1 2D Fuel Assembly

The first step in generating the cross-sections was to model a 2D fuel assembly in Serpent using reflective boundary conditions to represent it being surrounded by other assemblies. The output of such an assembly is treated as an input to a single node in DYN3D, where everything inside is homogenized to generate the cross-sections. Before 3D fuel assembly comparisons were performed, the output of various combinations of such 2D fuel assemblies were analyzed with respect to multiplication factor as a function of burnup to verify sensible results. See below for these results.

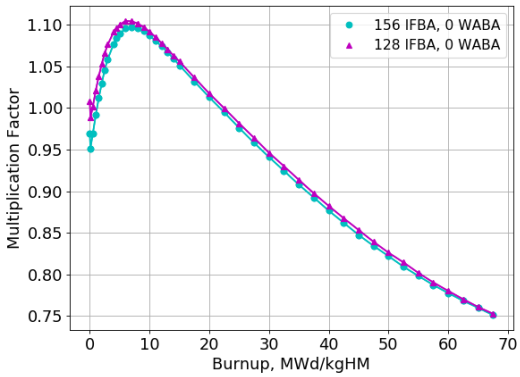

(a) 4.0% enriched fuel

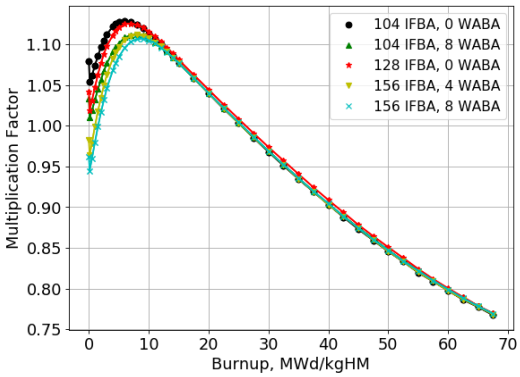

(b) 4.4% enriched fuel

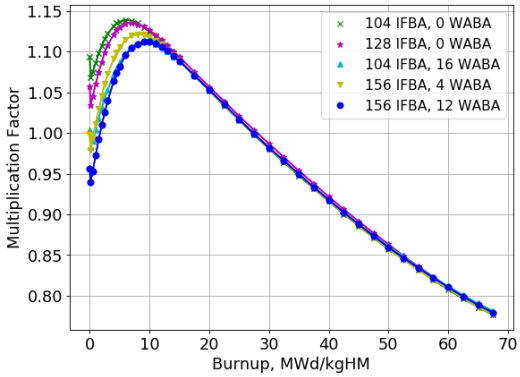

(c) 4.6% enriched fuel

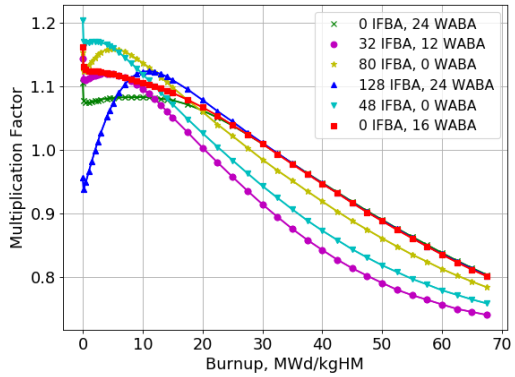

(d) 4.95% enriched fuel

Figure 5-1 Multiplication factor as a function of burnup for 4.0%, 4.4%, 4.6%, and 4.95% enriched 2D fuel assemblies with various burnable absorber configurations

The results of the 2D fuel assembly modeling are in accordance with expected assembly trends. In particular, the effects of the burnable absorbers can clearly be seen in Figure 5-1d, where the multiplication factor experiences a sharp increase to a peak, which once again begins to decline as the IFBA material is completely burned. There is a clear difference between the cases with many burnable absorbers and the cases with 0 IFBA rods, where the multiplication factor does not experience an initial increase.

5.1.2 3D Fuel Assembly

The nature of DYN3D requires single cross-sectional input files for each node. The cross-sections were homogenized in Serpent for each particular layer type with the following methodology:

- For active fuel regions, two iterations of the same approach were used. Central fuel layer cross-sections were generated from 2D assemblies similar to those described in *5.1.1*. The same approach was used for the blanket fuel layer cross-sections with minor geometry changes such as the exclusion of WABA rods and use of annular fuel pellets in IFBA rods.
- Group constants for the reflector regions were generated using supercell models as show in Figure 5-3. In Serpent, the reflector assembly material was surrounded by a model fuel assembly and cross-sections were generated for the central reflector universe.

See Figures 5-2 and 5-3 for depictions of the 3D fuel assembly model as well as the supercell configuration used to generate reflector cross sections.

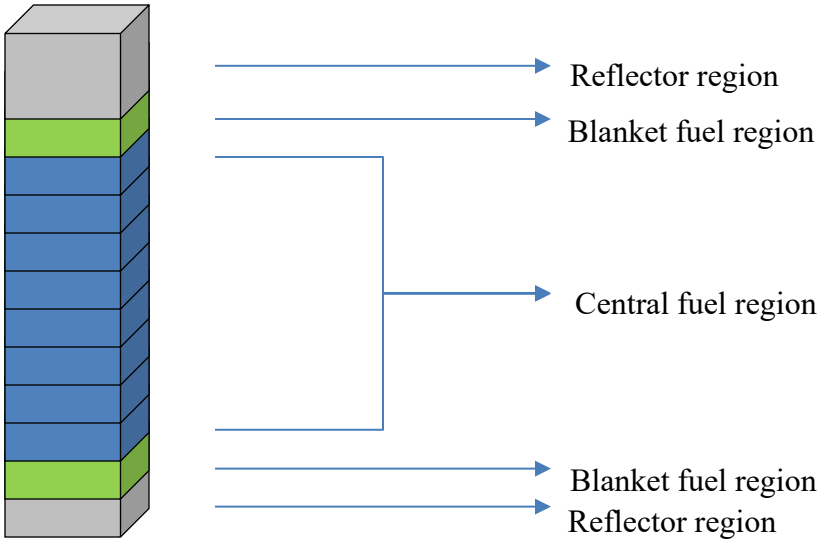

Figure 5-2 Axial geometry view of 3D fuel assembly for Buzz Unit 1

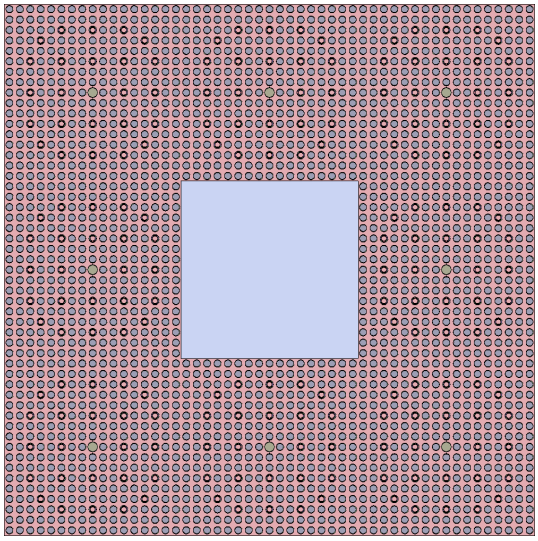

Figure 5-3 Reflector assembly supercell model

5.2 Results

5.2.1 3D Fuel Assembly

The first verification case between Serpent and DYN3D was performed on a 3D fuel assembly with 4.95% enriched fuel, 0 IFBA rods, and 24 WABA rods. The primary

purpose of this particular analysis was to confirm the validity of using 2D-generated cross-sections as inputs to a 3D fuel assembly in DYN3D. Fuel cross-sections were generated using a 2D Serpent fuel assembly with reflective boundary conditions and reflector cross-sections were generated using the supercell model of Figure 5-3. The values were inputted into a 3D fuel assembly model in DYN3D that corresponded to a matching model in Serpent.

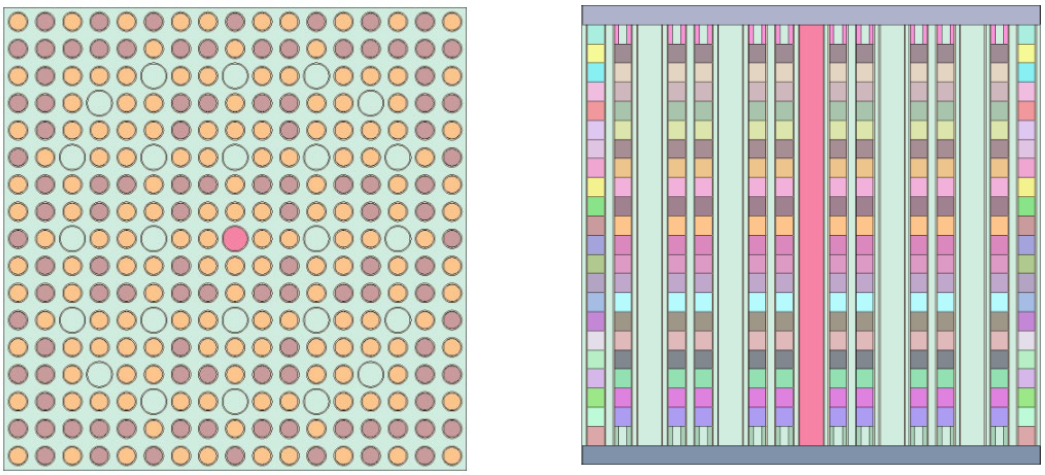

Figure 5-4 Serpent (L) Radial and (R) axial 3D fuel assembly geometry plots

Comparison metrics used were multiplication factor, power peaking as a function of axial height, and RMS power peaking as a function of axial height. All three metrics demonstrated very good agreement.

Table 5-1 Serpent vs. DYN3D for 3D fuel assembly

Serpent	DYN3D	Difference in pcm
1.21086 ± 2.1e-04	1.208826	-139.0

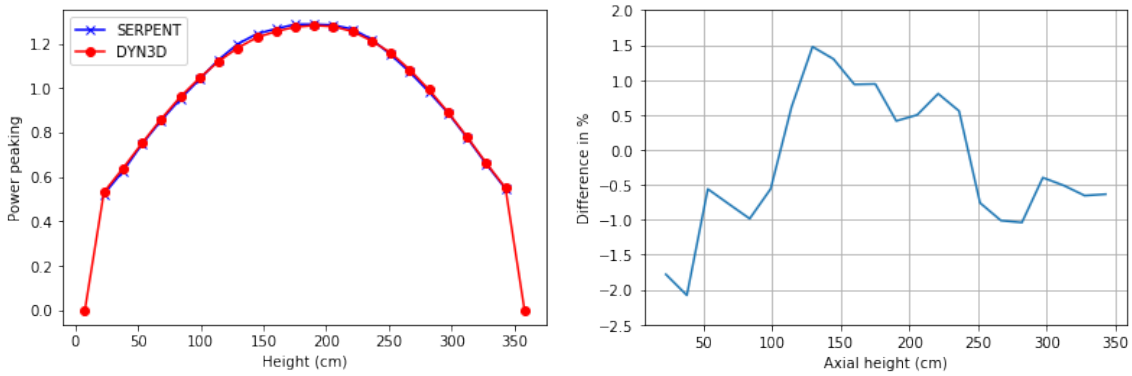

Figure 5-5 Axial power peaking and RMS power peaking for 3D fuel assembly comparison between Serpent and DYN3D

5.2.2 3D Fuel Assembly T/H Perturbations

A second verification case was performed on a different fuel assembly with 4.0% enriched fuel, 156 IFBA rods, and 0 WABA rods, as show in Figure 5-6.

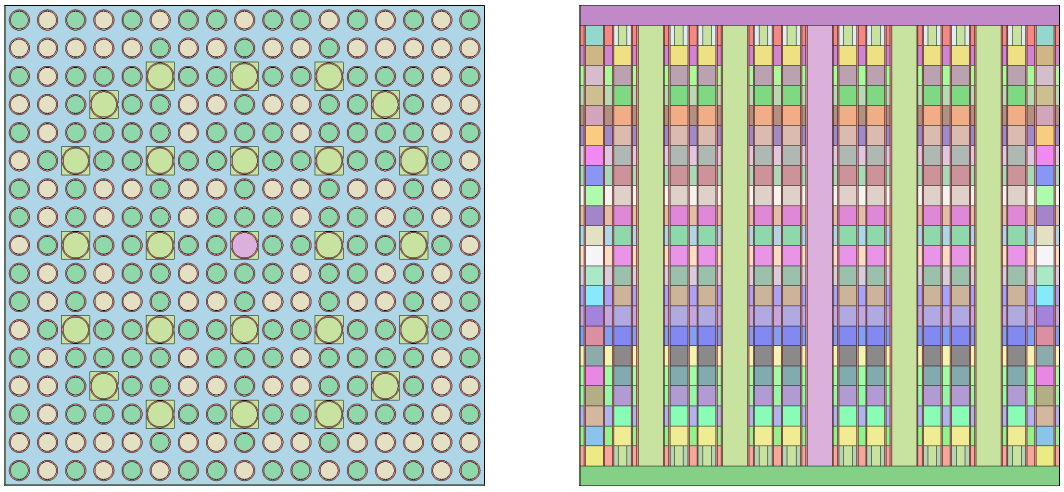

Figure 5-6 (L) Radial and (R) axial 3D fuel assembly geometry plots – 156 IFBA rods, 0 WABA rods

In this case, the coolant density was axially perturbed in each layer to simulate typical PWR assembly trends. In the previous reference cases, coolant density was taken

to be an average of 701.468 kg/m^3, but varied between 648.968 kg/m^3 and 753.968 kg/m^3 in increments of 5 for this case. Highest density was at the bottom and lowest was at the top, and all other T/H parameters were held constant. Once again, results demonstrated excellent agreement.

Table 5-2 Serpent vs. DYN3D for a 3D fuel assembly with axially varying coolant density

Serpent	DYN3D	Difference in pcm
0.885726 ± 2.5e-04	0.884836	-113.6

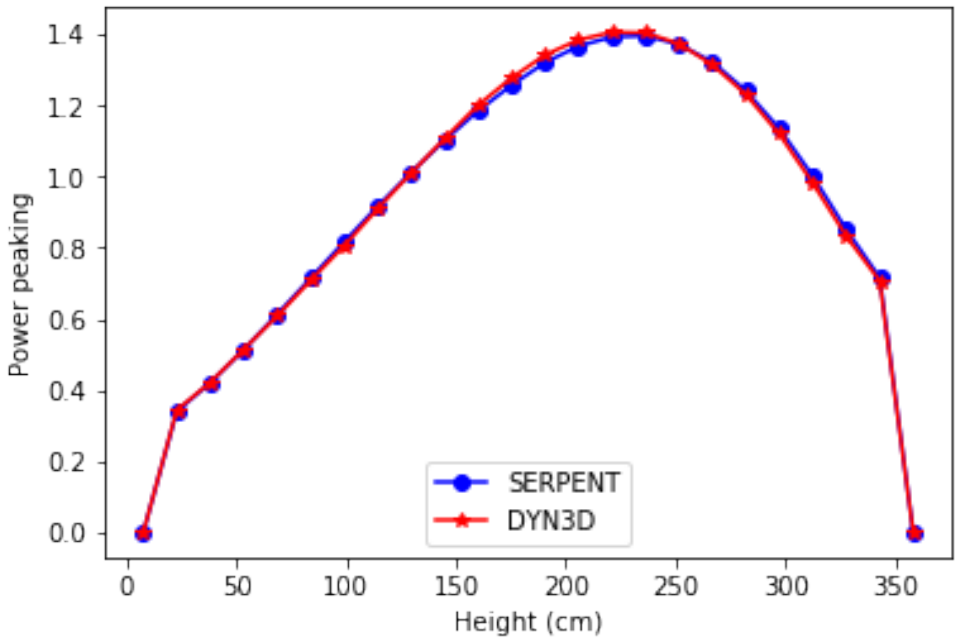

Figure 5-7 Axial power peaking difference between Serpent and DYN3D for axially varying coolant density

5.2.3 2D Full Core Comparison

Core loading maps and patterns were used to perform 2D core analyses for both a fresh and a 3-batch core. Each core was modeled in both Serpent and DYN3D with the primary goal of comparing parameters of multiplication factor and radial power peaking.

In the first case, all assemblies are fresh, i.e. the burnup distribution is uniform and equal to zero. Figure 5-8a presents the Serpent model, which relies on Cycle 48. Fresh assemblies are colored red, once-burned in blue, and twice-burned in yellow in the geometry plot. Figure 5-8b demonstrates the mesh plot, in which the blue color scheme shows thermal versus fast neutrons while the red color scheme shows power peaking.

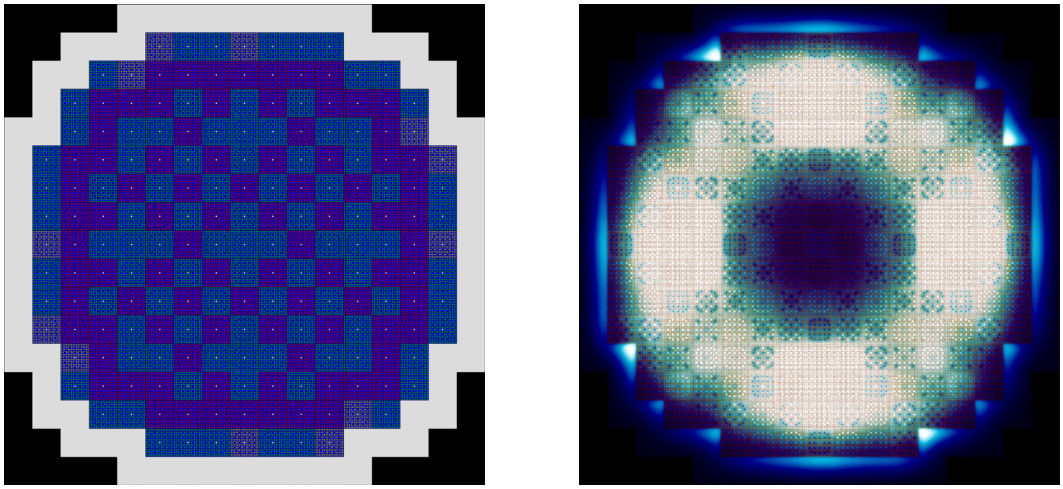

(a) Radial geometry plot (b) Radial mesh plot

Figure 5-8 Fresh core radial geometry and mesh plots

Table 5-3 Multiplication factor Serpent vs. DYN3D for 2D full core, fresh

Serpent	DYN3D	Difference in pcm
1.02381 ± 2.1e-05	1.022841	-92.5

For the fresh comparison, the values of multiplication factor for Serpent and DYN3D were within excellent agreement, i.e., within 92.5 pcm. The radial power peaking distribution comparing the two is plotted separately as well as on the same figure as difference in percent. The maximum difference remained within +2 and -8 percent, again demonstrating very good agreement between the two. The RMS difference in power peaking was around 2%.

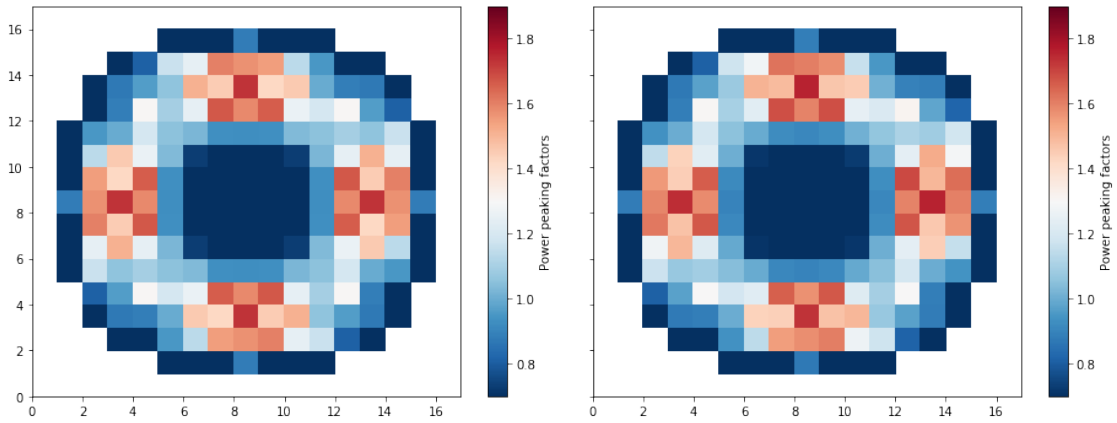

Figure 5-9 Fresh core power peaking between (L) Serpent and (R) DYN3D

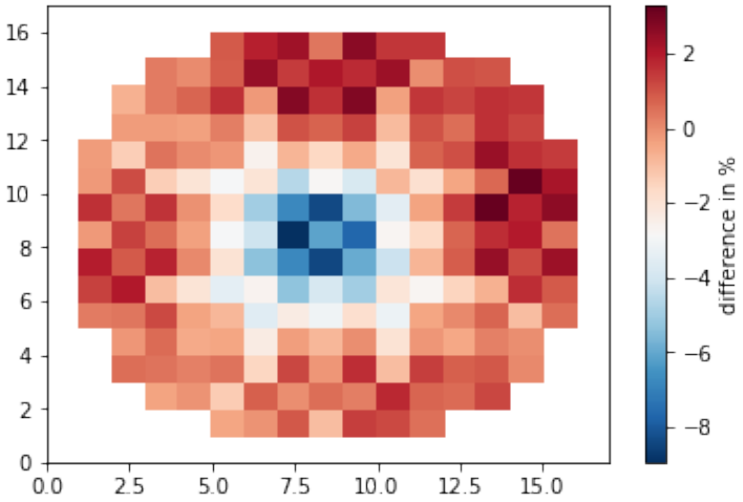

Figure 5-10 RMS power peaking difference by percent between Serpent and DYN3D

In order to perform simulations of the 3-batch core, the material compositions that corresponded to a specific burnup were used explicitly in Serpent in the files to generate cross-sections. The burned case took burnable materials (fuel, IFBA, and WABA) from output files of 2D assembly cases at specific burnup steps corresponding to the assembly in question. For example, the fuel material used in a once-burned assembly in the 3-batch core could have been taken from a file that corresponded to a burnup of 17 MWd/kgU,

whereas the same assembly in the fresh core model would have just used the fresh materials.

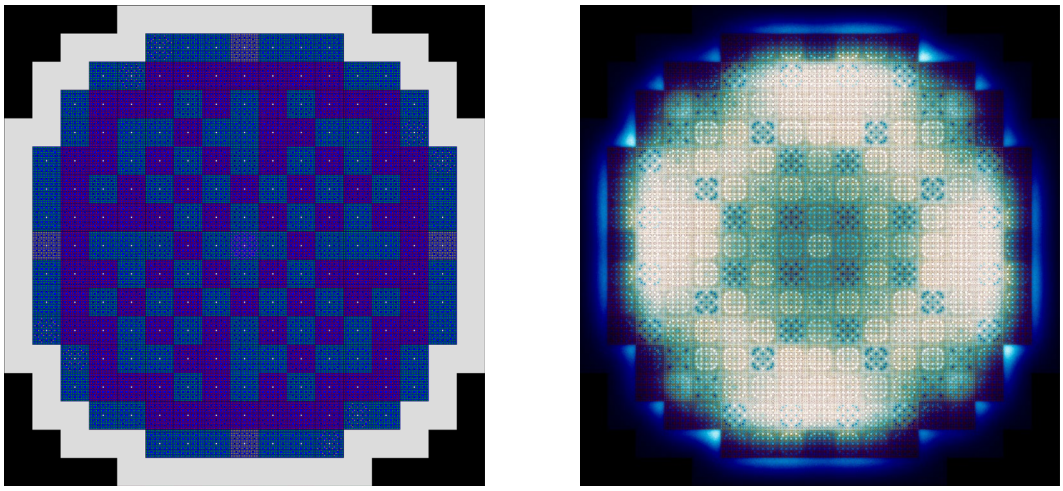

(a) Radial geometry plot (b) Radial mesh plot

Figure 5-11 3-batch core radial geometry and mesh plots

Table 5-4 Multiplication factor Serpent vs. DYN3D for 2D full core, 3-batch

Serpent	DYN3D	Difference in pcm
0.99241 ± 3.0e-05	0.99152	-90.4

The multiplication factor values for the 3-batch case were again in excellent agreement with the reference solution, resulting in a difference of only 90.4 pcm. Again, radial power peaking was compared, where it varied between ±4 percent, as seen in Figure 5-13.

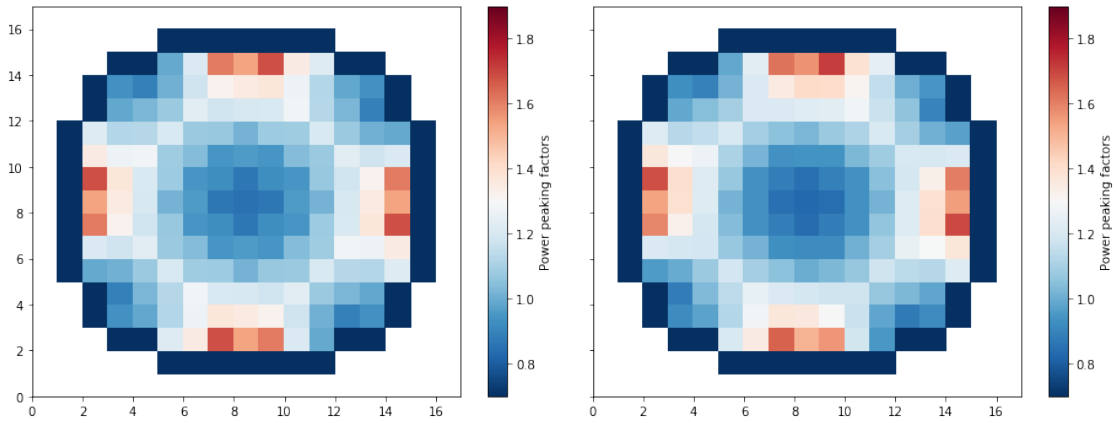

Figure 5-12 3-batch core power peaking comparison between Serpent and DYN3D

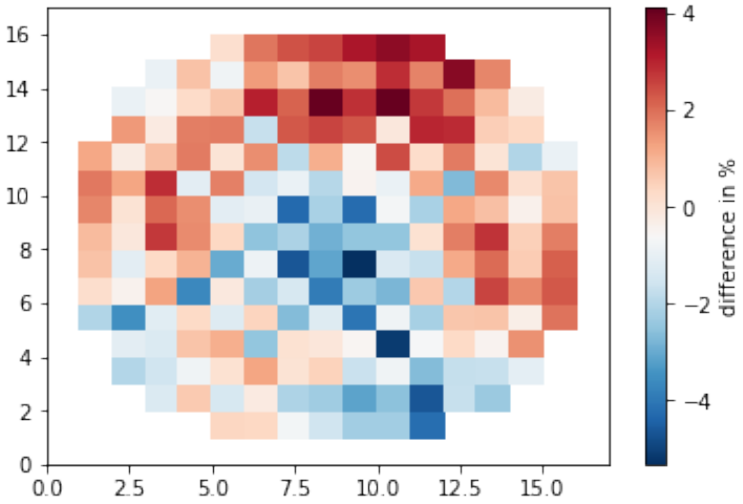

Figure 5-13 Power peaking difference by percent between Serpent and DYN3D

5.3 Discussion of Results

The first stage in verifying trends in the 2D assembly cases demonstrated expected outputs. Multiplication factor varied with enrichment and the effects of burnable absorbers could clearly be seen. The first comparison between Serpent and DYN3D for a 3D fuel assembly presented very good agreement, and axial power peaking was within around 2% difference. A second comparison was done with axially varying coolant density, which

once again show excellent agreement in power peaking and multiplication factor with a difference of 113.6 pcm. The final stage was a 2D core comparison for both fresh and 3-batch cores with metrics of multiplication factor and radial power peaking used. The respective differences in multiplication factor for each core were 92.5 and 90.4 pcm, and radial power peaking differences remained within a maximum of 8 percent. The notably good agreement from the sequence of these results therefore allowed us to move on to the next stage by verifying the compatibility of both codes when generating cross-sections for DYN3D from Serpent.

CHAPTER 6. SENSITIVITY STUDIES

This chapter presents the sensitivity studies performed to analyze the effects of number of energy groups and inclusion or exclusion of assembly discontinuity factors (ADFs) on differences between outputs of the two codes. Full core 2D models were created in both Serpent and DYN3D with fuel assemblies and peripheral reflectors. The comparison metrics used were multiplication factor and difference in power peaking. The combinations of fresh versus 3-batch core with two or eight energy groups and with or without ADFs resulted in eight different cases which will be presented in the following sections.

6.1 Overview

Reactor cores are systems that often involve high levels of spatial heterogeneity resulting from different geometries and materials. Since nodal diffusion codes by nature homogenize spatial regions of interest (nodes), boundaries are created at which there can be flux discontinuities [20]. One way to account for this is with assembly discontinuity factors (ADFs), which are the ratio of heterogeneous surface flux to homogeneous flux at adjacent nodes [21]. The studies performed in this section determine whether the system under consideration obtains better results with or without these correction factors.

Also included in this investigation is two sets of energy groups. The choice of energy boundaries in reactor physics codes is important in solving the transport equation, thus two common energy structures were chosen to factor into the inputs as well as the inclusion or exclusion of ADFs [22].

6.2 2 Energy Groups

The first case presented is that for two energy groups without ADFs and both fresh and 3-batch cores. For both cases of 2 energy groups, a typical thermal cutoff of 0.625 eV was used as the boundary.

Table 6-1 Serpent vs. DYN3D, 2 groups and no ADFs

	Serpent	DYN3D	Difference in pcm
Fresh	1.02385 ± 2.1e-05	1.022875	-93.1
3-batch	0.992711 ± 1.9e-05	0.992167	-55.2

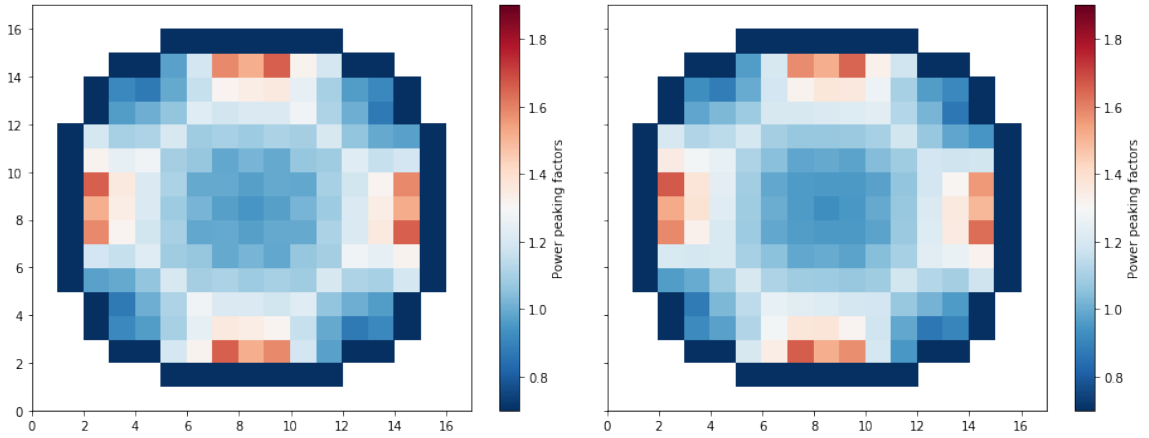

Figure 6-1 Core power peaking comparison between Serpent and DYN3D, 2 groups, no ADFs

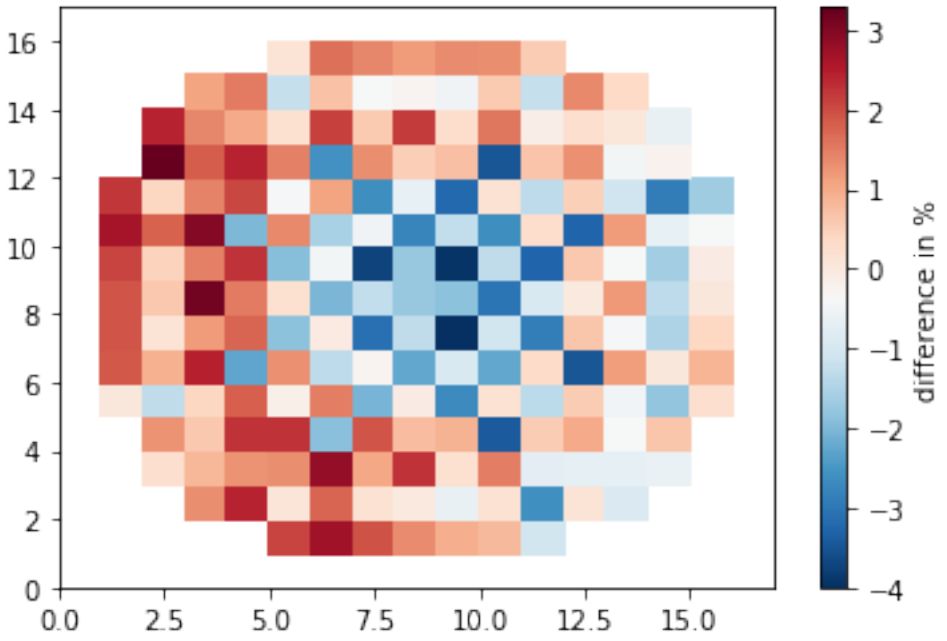

Figure 6-2 Power peaking difference by percent between Serpent and DYN3D, 2 groups, no ADFs

The second case presented is that for two energy groups with ADFs and both fresh and 3-batch cores.

Table 6-2 Serpent vs. DYN3D, 2 groups with ADFs

	Serpent	DYN3D	Difference in pcm
Fresh	1.02385 ± 2.1e-05	1.022488	-130.1
3-batch	0.992723 ± 1.9e-05	0.992063	-67.0

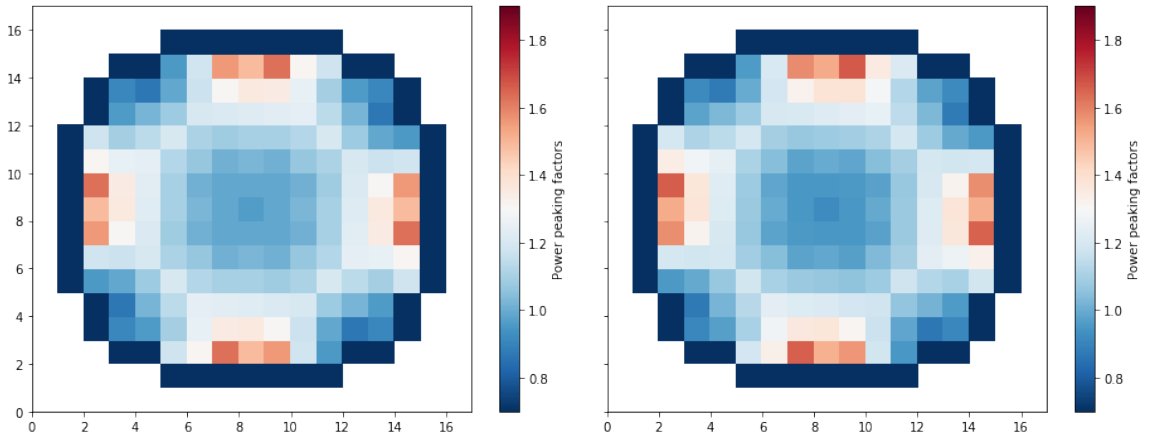

Figure 6-3 Core power peaking comparison between Serpent and DYN3D, 2 groups with ADFs

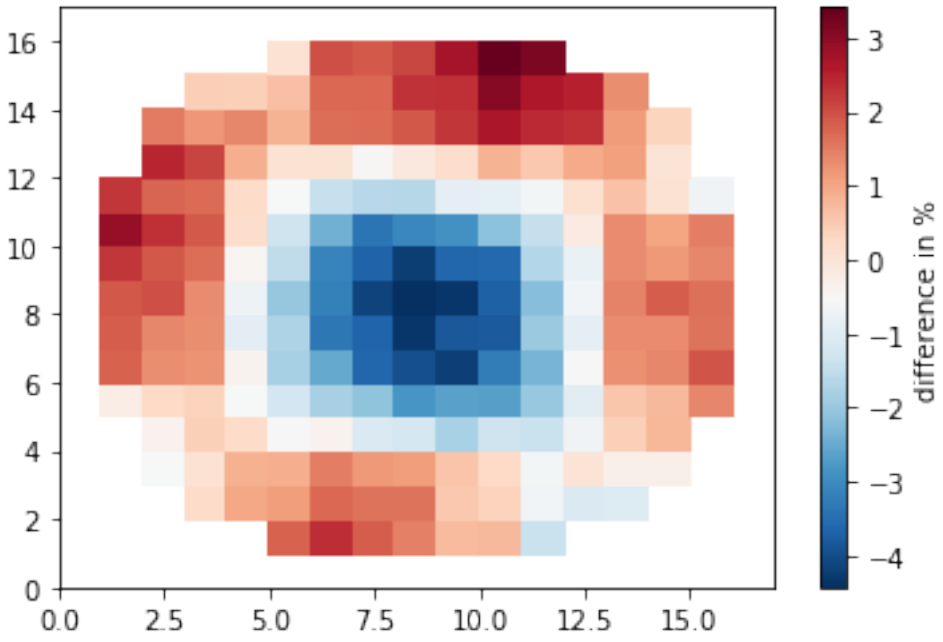

Figure 6-4 Power peaking difference by percent between Serpent and DYN3D, 2 groups with ADFs

6.3 8 Energy Groups

The third case presented is that for eight energy groups without ADFs and both fresh and 3-batch cores. The following energy cutoffs (MeV) were used for the boundaries in both of the following cases.

Table 6-3 Energy boundary cutoffs (MeV) for 8-group structure

1	1.4572E-07	5	9.1188E-03
2	6.2506E-07	6	8.2085E-01
3	3.9279E-06	7	2.2313E+00
4	1.3007E-04		

Table 6-4 Serpent vs. DYN3D, 8 groups and no ADFs

	Serpent	DYN3D	Difference in pcm
Fresh	1.02384 ± 2.1e-05	1.022014	-174.5
3-batch	0.992734 ± 1.8e-05	0.991735	-101.5

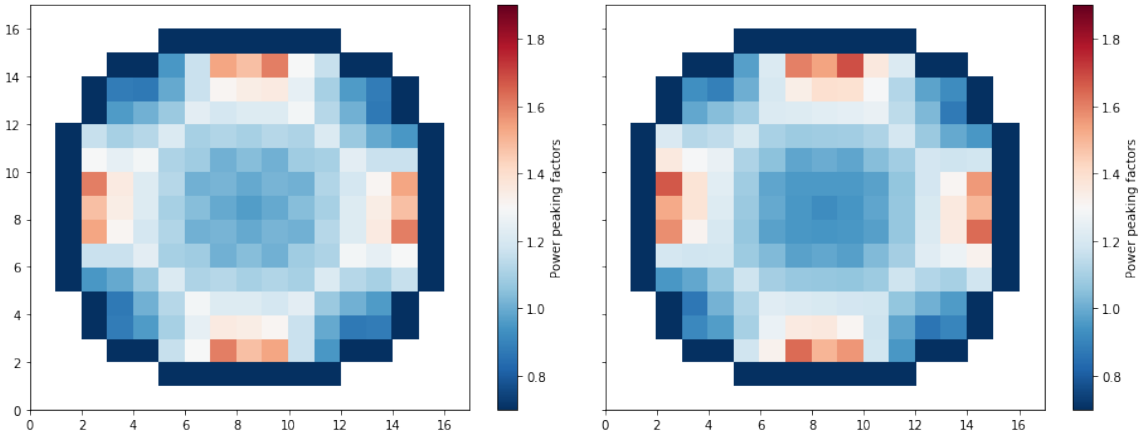

Figure 6-5 Core power peaking comparison between Serpent and DYN3D, 8 groups, no ADFs

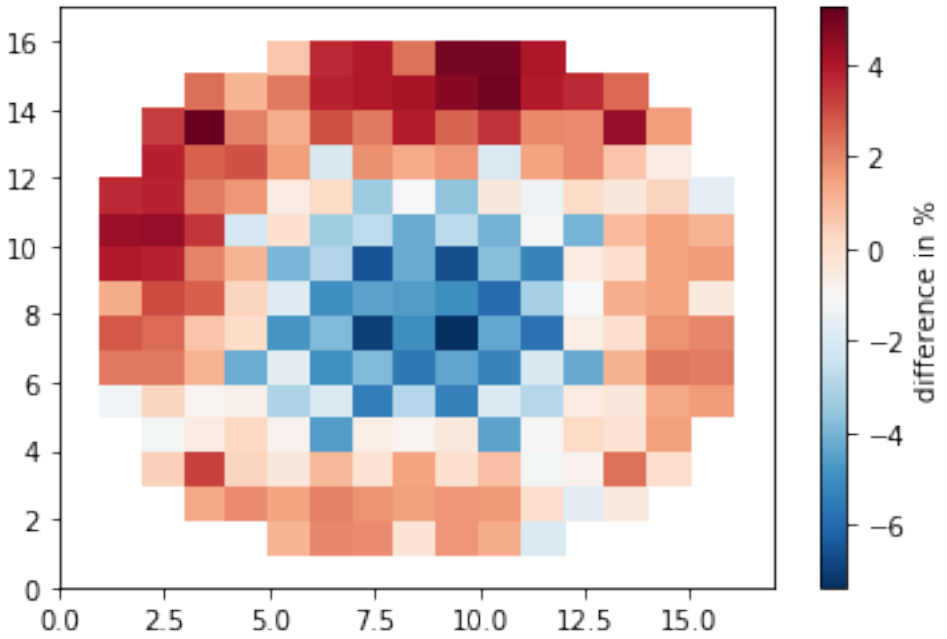

Figure 6-6 Power peaking difference by percent between Serpent and DYN3D, 8 groups, no ADFs

The third case presented is that for eight energy groups with ADFs and both fresh and 3-batch cores.

Table 6-5 Serpent vs. DYN3D, 8 groups with ADFs

	Serpent	DYN3D	Difference in pcm
Fresh	1.02384 ± 2.1e-05	1.021693	-205.2
3-batch	0.99271 ± 1.9e-05	0.991628	-109.9

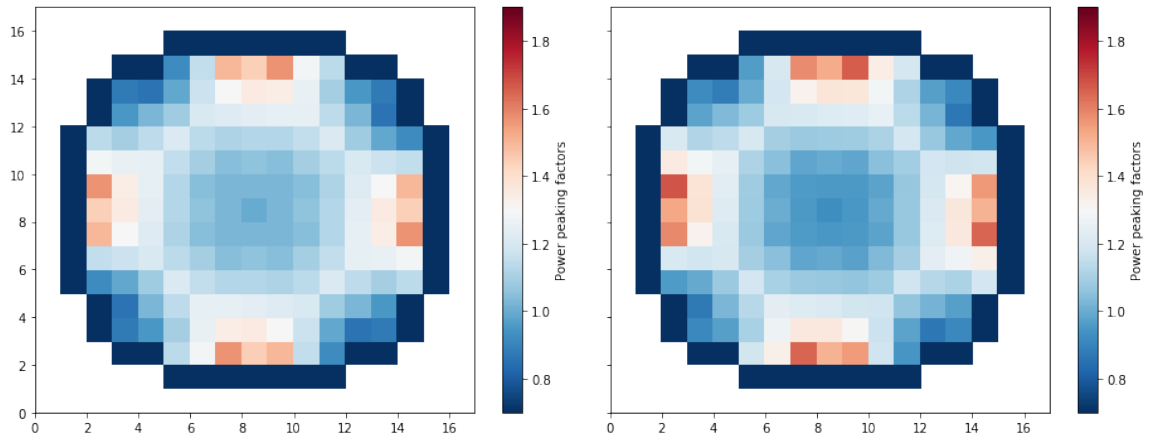

Figure 6-7 Core power peaking comparison between Serpent and DYN3D, 8 groups with ADFs

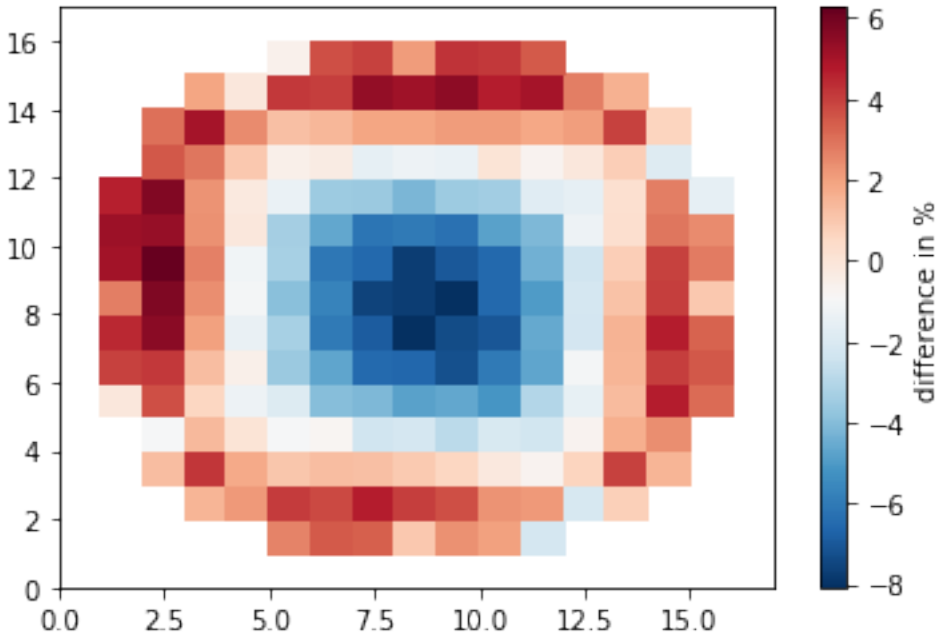

Figure 6-8 Power peaking difference by percent between Serpent and DYN3D, 8 groups, with ADFs

6.4 Discussion of Results

The purpose of this study was to compare the compatibility of Serpent and DYN3D with various group constant input parameters. The results consistently demonstrate better

agreement between the 3-batch core cases than the fresh cases, which was also seen in the initial comparison case in Chapter 5. It is also worth noting the systematically lower values of multiplication factor between the fresh and 3-batch cores, which is expected. For both 2-groups and 8-groups, the cases without ADFs both result in less error, which could be attributed to a lower degree of heterogeneity than, say, a core with varying fuel types. Finally, the 2-group cases demonstrate the best comparison, thus the 2-group case with no ADFs was chosen for the rest of the work. It is possible that the addition of reflectors at the upper and lower periphery of the core could add higher levels of heterogeneity and make the ADFs beneficial, but the reflectors were placed only on the radial periphery in the 2D core case.

CHAPTER 7. EQUILIBRIUM AND BENCHMARK CYCLES

This chapter presents the final portion of the analysis concerned with replicating the equilibrium cycle from given data. First, an overview of equilibrium cycles and their importance is described. Next, the loading and shuffling maps to perform the analyses are presented. Most of the data relies on publicly available literature concerning the methods of modeling IFBA [26], a plant data document [1], and an overview of a reflector model [27], all based on a Westinghouse 4-loop plant. The EOC jumpstart is generated for Buzz Unit 1 Cycle 45. Cycles 48, 49, and 50 are designated as benchmark cycles and Cycles 46 and 47 are considered catch-up cycles for the benchmarks. The primary focuse of the analyses was performed on Cycle 48, as this was the case with the most known information and thus easiest to closely model. Finally, the specific methodology and subsequent results are presented.

7.1 Equilibrium Analysis Overview

Current LWR fuel management involves the use of multi-batch loading patterns where fuel assemblies are loaded into the core in several stages. That is, at each point in time, the core will contain a certain number of fresh, once-, and twice-burned fuel assemblies.

An equilibrium cycle is a steady-state loading pattern with fixed values of fresh fuel assemblies, feed batch enrichment, number of burnable absorbers, and fuel reloading [23]. As a result, core characteristics of cycle length and discharge burnup are identical in

consecutive cycles. The equilibrium cycle is converged on by an iteration of steady-state burnup simulations where assembly reloading patterns are the same in successive cycles.

Analysis of equilibrium cycles is particularly useful in evaluating new fuels and defining operating parameters in a core containing them, as well as evaluating the economic and safety features of newly defined fuel assemblies. In this work, the goal of the equilibrium analysis is to converge on a comparable solution to that given in the plant document with respect to cycle length and discharge burnup. This benchmark would be a validation of the sequence, and the equilibrium setup could then be used to model new cycles – in particular, a HALEU core.

7.2 Fuel Management

A 3-batch loading scheme is adopted for all core configurations presented here, and the enrichment of UO_2 is below 5 w/o ^{235}U. A total of 193 fuel assemblies are loaded into the core and the reflector is converted to 64 fuel assemblies that surround the active core resulting in a total of 257 assemblies within the core. The number of assemblies per reload for each of the cycles is presented in Table 7-1. In general, a low-leakage pattern is adopted for all of the cycles. This is achieved by positioning the twice-burned assemblies at the outermost peripheral locations, which surround a checkerboard configuration of fresh and once-burned assemblies. The power distribution is balanced by the inclusion of burnable absorbers. The loading maps are described separately for each cycle in Figures 7-1 through 7-5 and detailed shuffling schemes for each of the cycles are presented in Tables 7-2 through 7-3. Assemblies that were not identified are denoted as ‘XXXX’ and the colors indicate fresh, once-burned, and twice-burned fuels.

Table 7-1 Number of fresh feed assemblies for each cycle

No. Fresh Assemblies	
Cycle 46	85
Cycle 47	92
Cycle 48	100
Cycle 49	93
Cycle 50	100

For each cycle, three forms of assembly information are provided. First is a core loading table with assembly keys and corresponding values of enrichment, IFBA rods, WABA rods, and heavy metal loading for each unique assembly. The second table given contains feed batch, central zone, and fuel assembly IDs that match with adjacent reload maps. These are depicted in the first plots of Figures 7-1 to 7-5 but were converted into the formats seen in the second plots to match the assembly keys given in the core loading table.

	R	P	N	M	L	K	J	H	G	F	E	D	C	B	A
1					6F82	6G08	6F09	6G91	6F11	6G27	6F81				
2			6G67	6G54	6H75	6H31	6H67	6H54	6H69	6H33	6H77	6G59	6G68		
3		6G62	6H82	6H40	6H03	6G20	6H08	6G33	6H10	6G32	6H19	6H43	6H83	6G72	
4		6G60	6H45	6G66	6G82	6H51	6G57	6G37	6G56	6H52	6G88	6G71	6H39	6G53	
5	6F84	6H78	6H20	6G84	6G14	6G43	6H59	6G01	6H61	6G42	6G16	6G89	6H02	6H79	6F79
6	6G21	6H34	6G24	6H53	6G45	6H24	6G81	6H04	6G76	6H14	6G40	6H41	6G30	6H35	6G11
7	6F02	6H70	6H15	6G58	6H62	6G79	6H26	6G09	6H27	6G78	6H63	6G46	6H11	6H71	6F10
8	6G90	6H55	6G17	6G36	6G02	6H12	6G06	6H07	6G07	6H09	6G03	6G35	6G25	6H56	6G93
9	6F08	6H72	6H01	6G51	6H64	6G74	6H28	6G05	6H29	6G80	6H58	6G48	6H18	6H66	6F07
10	6G10	6H36	6G23	6H48	6G39	6H06	6G75	6H05	6G77	6H23	6G41	6H49	6G31	6H30	6G19
11	6F78	6H80	6H22	6G85	6G13	6G38	6H65	6G04	6H60	6G44	6G15	6G83	6H17	6H74	6F80
12		6G52	6H46	6G69	6G87	6H47	6G49	6G34	6G61	6H42	6G86	6G70	6H44	6G55	
13		6G64	6H84	6H38	6H25	6G22	6H16	6G26	6H13	6G29	6H21	6H50	6H85	6G73	
14			6G63	6G50	6H81	6H37	6H73	6H57	6H68	6H32	6H76	6G47	6G65		
15					6F77	6G18	6F03	6G92	6F05	6G12	6F83				

	R	P	N	M	L	K	J	H	G	F	E	D	C	B	A
1					XXXX	XXXX	XXXX	XXXX	XXXX	XXXX	XXXX				
2			XXXX	XXXX	48C3	48B1	48C2	48B2	48C2	48B1	48C3	XXXX	XXXX		
3		XXXX	48C1	48B4	48A1	XXXX	48A1	XXXX	48A1	XXXX	48A1	48B4	48C1	XXXX	
4		XXXX	48B4	XXXX	XXXX	48B4	XXXX	XXXX	XXXX	48B4	XXXX	XXXX	48B4	XXXX	
5	XXXX	48C3	48A1	XXXX	XXXX	XXXX	48B5	XXXX	48B5	XXXX	XXXX	XXXX	48A1	48C3	XXXX
6	XXXX	48B1	XXXX	48B4	XXXX	48A1	XXXX	48A1	XXXX	48A1	XXXX	48B4	XXXX	48B1	XXXX
7	XXXX	48C2	48A1	XXXX	48B5	XXXX	48B3	XXXX	48B3	XXXX	48B5	XXXX	48A1	48C2	XXXX
8	XXXX	48B2	XXXX	XXXX	XXXX	48A1	XXXX	48A1	XXXX	48A1	XXXX	XXXX	XXXX	48B2	XXXX
9	XXXX	48C2	48A1	XXXX	48B5	XXXX	48B3	XXXX	48B3	XXXX	48B5	XXXX	48A1	48C2	XXXX
10	XXXX	48B1	XXXX	48B4	XXXX	48A1	XXXX	48A1	XXXX	48A1	XXXX	48B4	XXXX	48B1	XXXX
11	XXXX	48C3	48A1	XXXX	XXXX	XXXX	48B5	XXXX	48B5	XXXX	XXXX	XXXX	48A1	48C3	XXXX
12		XXXX	48B4	XXXX	XXXX	48B4	XXXX	XXXX	XXXX	48B4	XXXX	XXXX	48B4	XXXX	
13		XXXX	48C1	48B4	48A1	XXXX	48A1	XXXX	48A1	XXXX	48A1	48B4	48C1	XXXX	
14			XXXX	XXXX	48C3	48B1	48C2	48B2	48C2	48B1	48C3	XXXX	XXXX		
15					XXXX	XXXX	XXXX	XXXX	XXXX	XXXX	XXXX				

Figure 7-1 Loading maps for Cycle 46 – catch-up cycle; fresh fuel, once-burned, and twice-burned fuel are denoted by the green, blue, and red colors

	R	P	N	M	L	K	J	H	G	F	E	D	C	B	A
1					6G18	6H03	6H11	6H38	6G64	6G63	6G92				
2			6H74	6H72	6J78	6J30	6J66	6J45	6J68	6J32	6J80	6H66	6H80		
3		6H76	6J73	6J50	6J03	6H09	6J10	6H55	6J12	6H16	6J21	6J52	6J74	6H81	
4		6H69	6J53	6H82	6H64	6J38	6H20	6J22	6H14	6J40	6H58	6H83	6J54	6H67	
5	6G93	6J81	6J02	6H61	6J89	6H27	6J58	6H47	6J60	6H51	6J90	6H59	6J27	6J82	6G21
6	6G73	6J33	6H18	6J41	6H48	6J05	6H33	6J16	6H31	6J17	6H29	6J42	6H05	6J34	6H02
7	6G65	6J69	6J13	6H24	6J61	6H36	6J85	6H40	6J86	6H30	6J62	6H19	6J14	6J70	6H13
8	6H44	6J46	6H57	6J09	6H49	6J11	6H46	6H07	6H39	6J01	6H53	6J20	6H54	6J47	6H45
9	6H08	6J71	6J08	6H25	6J63	6H34	6J87	6H50	6J88	6H35	6J57	6H23	6J07	6J65	6G67
10	6H22	6J35	6H04	6J43	6H26	6J25	6H32	6J24	6H37	6J19	6H41	6J37	6H15	6J29	6G62
11	6G19	6J83	6J28	6H60	6J91	6H42	6J64	6H52	6J59	6H28	6J92	6H65	6J18	6J77	6G90
12		6H68	6J55	6H84	6H62	6J44	6H06	6J15	6H17	6J39	6H63	6H85	6J49	6H73	
13		6H77	6J75	6J56	6J23	6H10	6J06	6H56	6J26	6H12	6J04	6J51	6J76	6H75	
14			6H79	6H70	6J84	6J36	6J72	6J48	6J67	6J31	6J79	6H71	6H78		
15					6G91	6G68	6G72	6H43	6H01	6H21	6G27				

	R	P	N	M	L	K	J	H	G	F	E	D	C	B	A
1					XXXX	48A1	48A1	48B4	XXXX	XXXX	XXXX				
2			48C3	48C2	49C5	49B1	49C1	49B3	49C1	49B1	49C5	48C2	48C3		
3		48C3	49C3	49B4	49A1	48A1	49A1	48B2	49A1	48A1	49A1	49B4	49C3	48C3	
4		48C2	49B4	48C1	48B5	49B2	48A1	49A1	48A1	49B2	48B5	48C1	49B4	48C2	
5	XXXX	49C5	49A1	48B5	49C7	48B3	49B5	48B4	49B5	48B4	49C7	48B5	49A1	49C5	XXXX
6	XXXX	49B1	48A1	49B2	48B4	49A1	48B1	49A1	48B1	49A1	48B3	49B2	48A1	49B1	48A1
7	XXXX	49C1	49A1	48A1	49B5	48B1	49C6	48B4	49C6	48B1	49B5	48A1	49A1	49C1	48A1
8	48B4	49B3	48B2	49A1	48B4	49A1	48B4	48A1	48B4	49A1	48B4	49A1	48B2	49B3	48B4
9	48A1	49C1	49A1	48A1	49B5	48B1	49C6	48B4	49C6	48B1	49B5	48A1	49A1	49C1	XXXX
10	48A1	49B1	48A1	49B2	48B3	49A1	48B1	49A1	48B1	49A1	48B4	49B2	48A1	49B1	XXXX
11	XXXX	49C5	49A1	48B5	49C7	48B4	49B5	48B4	49B5	48B3	49C7	48B5	49A1	49C5	XXXX
12		48C2	49B4	48C1	48B5	49B2	48A1	49A1	48A1	49B2	48B5	48C1	49B4	48C2	
13		48C3	49C3	49B4	49A1	48A1	49A1	48B2	49A1	48A1	49A1	49B4	49C3	48C3	
14			48C3	48C2	49C5	49B1	49C1	49B3	49C1	49B1	49C5	48C2	48C3		
15					XXXX	XXXX	XXXX	48B4	48A1	48A1	XXXX				

Figure 7-2 Loading maps for Cycle 47 – catch-up cycle; fresh fuel, once-burned, and twice-burned fuel are denoted by the green, blue, and red colors

	R	P	N	M	L	K	J	H	G	F	E	D	C	B	A
1					6J21	6J17	6J01	6H71	6J26	6J07	6H77				
2			6J09	6J56	6K70	6K42	6K78	6K29	6K80	6K44	6K72	6H79	6J03		
3		6J28	6K85	6K50	6K07	6J71	6K12	6J31	6K14	6J65	6K23	6K52	6K86	6J22	
4		6H75	6K53	6J73	6J46	6K34	6J89	6J36	6J86	6K36	6J54	6J74	6K54	6J53	
5	6H78	6K73	6K24	6J50	6K01	6J39	6K58	6J84	6K60	6J44	6K02	6J45	6K06	6K74	6J18
6	6J12	6K45	6J68	6K37	6J37	6K27	6J61	6K08	6J62	6K18	6J43	6K38	6J66	6K46	6J19
7	6J14	6K81	6K19	6J85	6K61	6J58	6K66	6J78	6K67	6J60	6K57	6J90	6K15	6K82	6J24
8	6H67	6K30	6J34	6J29	6J77	6K16	6J83	6T52	6J82	6K11	6J81	6J33	6J35	6K31	6H68
9	6J16	6K83	6K13	6J91	6K68	6J64	6K59	6J79	6K64	6J59	6K65	6J88	6K05	6K77	6J08
10	6J05	6K47	6J67	6K39	6J42	6K22	6J63	6K10	6J57	6K09	6J41	6K33	6J72	6K41	6J06
11	6J02	6K75	6K26	6J48	6K03	6J40	6K62	6J80	6K63	6J38	6K04	6J51	6K25	6K69	6H74
12		6J49	6K55	6J75	6J55	6K40	6J87	6J32	6J92	6K35	6J47	6J76	6K49	6H76	
13		6J15	6K87	6K56	6K21	6J69	6K28	6J30	6K20	6J70	6K17	6K51	6K88	6J27	
14			6J04	6H80	6K76	6K48	6K84	6K32	6K79	6K43	6K71	6J52	6J20		
15					6H81	6J13	6J10	6H72	6J11	6J25	6J23				

	R	P	N	M	L	K	J	H	G	F	E	D	C	B	A
1					49A1	49A1	49A1	48C2	49A1	49A1	48C3				
2			49A1	49B4	50C2	50B2	50C4	50B1	50C4	50B2	50C2	48C3	49A1		
3		49A1	50C1	50B4	50A2	49C1	50A2	49B1	50A2	49C1	50A2	50B4	50C1	49A1	
4		48C3	50B4	49C3	49B3	50B3	49C7	49B1	49C6	50B3	49B4	49C3	50B4	49B4	
5	48C3	50C2	50A2	49B4	50A1	49B2	50B5	49C5	50B5	49B2	50A1	49B3	50A2	50C2	49A1
6	49A1	50B2	49C1	50B3	49B2	50A2	49B5	50A2	49B5	50A2	49B2	50B3	49C1	50B2	49A1
7	49A1	50C4	50A2	49C6	50B5	49B5	50B5	49C5	50B5	49B5	50B5	49C7	50A2	50C4	49A1
8	48C2	50B1	49B1	49B1	49C5	50A2	49C5	XXXX	49C5	50A2	49C5	49B1	49B1	50B1	48C2
9	49A1	50C4	50A2	49C7	50B5	49B5	50B5	49C5	50B5	49B5	50B5	49C6	50A2	50C4	49A1
10	49A1	50B2	49C1	50B3	49B2	50A2	49B5	50A2	49B5	50A2	49B2	50B3	49C1	50B2	49A1
11	49A1	50C2	50A2	49B3	50A1	49B2	50B5	49C5	50B5	49B2	50A1	49B4	50A2	50C2	48C3
12		49B4	50B4	49C3	49B4	50B3	49C6	49B1	49C7	50B3	49B3	49C3	50B4	48C3	
13		49A1	50C1	50B4	50A2	49C1	50A2	49B1	50A2	49C1	50A2	50B4	50C1	49A1	
14			49A1	48C3	50C2	50B2	50C4	50B1	50C4	50B2	50C2	49B4	49A1		
15					48C3	49A1	49A1	48C2	49A1	49A1	49A1				

Figure 7-3 Loading maps for Cycle 48 – catch-up cycle; fresh fuel, once-burned, and twice-burned fuel are denoted by the green, blue, and red colors

	R	P	N	M	L	K	J	H	G	F	E	D	C	B	A
1					6J27	6K21	6K09	6J23	6K01	6K07	6J15				
2			6J19	6K33	7A75	7A31	7A83	7A33	7A85	7A34	7A77	6K38	6K54		
3		6K50	7A70	7A51	7A08	6K81	7A13	6K64	7A15	6K82	7A24	7A53	7A71	6J25	
4		6K34	7A54	6K85	6K60	7A43	6K46	6K56	6K45	7A45	6K63	6K86	7A55	6K40	
5	6J20	7A78	7A25	6K57	7A02	6K28	7A59	6K29	7A61	6K20	7A03	6K65	7A07	7A79	6J04
6	6K26	7A39	6K78	7A46	6K15	7A28	6K70	7A09	6K72	7A19	6K19	7A47	6K80	7A40	6K24
7	6K03	7A86	7A20	6K48	7A62	6K73	7A67	6K10	7A68	6K74	7A58	6K43	7A16	7A87	6K22
8	6J18	7A30	6K67	6K49	6K30	7A17	6K11	7A01	6K16	7A12	6K31	6K53	6K59	7A41	6J02
9	6K18	7A88	7A14	6K42	7A69	6K75	7A60	6K08	7A65	6K69	7A66	6K44	7A06	7A82	6K02
10	6K25	7A32	6K84	7A48	6K05	7A23	6K76	7A11	6K71	7A10	6K13	7A42	6K79	7A37	6K06
11	6J03	7A80	7A27	6K61	7A04	6K12	7A63	6K32	7A64	6K14	7A05	6K68	7A26	7A74	6J09
12		6K36	7A56	6K87	6K58	7A49	6K41	6K52	6K47	7A44	6K62	6K88	7A50	6K35	
13		6J17	7A72	7A57	7A22	6K83	7A29	6K66	7A21	6K77	7A18	7A52	7A73	6K51	
14			6K55	6K39	7A81	7A38	7A89	7A35	7A84	7A36	7A76	6K37	6J05		
15					6J22	6K17	6K04	6J21	6K27	6K23	6J28				

	R	P	N	M	L	K	J	H	G	F	E	D	C	B	A
1					49A1	50A2	50A2	49A1	50A1	50A2	49A1				
2			49A1	50B3	51C2	51B1	51C3	51B1	51C3	51B1	51C2	50B3	50B4		
3		50B4	51C1	51B3	51A4	50C4	51A4	50B5	51A4	50C4	51A4	51B3	51C1	49A1	
4		50B3	51B3	50C1	50B5	51B2	50B2	50B4	50B2	51B2	50B5	50C1	51B3	50B3	
5	49A1	51C2	51A4	50B5	51A2	50A2	51B4	50B1	51B4	50A2	51A2	50B5	51A4	51C2	49A1
6	50A2	51B1	50C4	51B2	50A2	51A4	50C2	51A4	50C2	51A4	50A2	51B2	50C4	51B1	50A2
7	50A1	51C3	51A4	50B2	51B4	50C2	51B4	50A2	51B4	50C2	51B4	50B2	51A4	51C3	50A2
8	49A1	51B1	50B5	50B4	50B1	51A4	50A2	51A1	50A2	51A4	50B1	50B4	50B5	51B1	49A1
9	50A2	51C3	51A4	50B2	51B4	50C2	51B4	50A2	51B4	50C2	51B4	50B2	51A4	51C3	50A1
10	50A2	51B1	50C4	51B2	50A2	51A4	50C2	51A4	50C2	51A4	50A2	51B2	50C4	51B1	50A2
11	49A1	51C2	51A4	50B5	51A2	50A2	51B4	50B1	51B4	50A2	51A2	50B5	51A4	51C2	49A1
12		50B3	51B3	50C1	50B5	51B2	50B2	50B4	50B2	51B2	50B5	50C1	51B3	50B3	
13		49A1	51C1	51B3	51A4	50C4	51A4	50B5	51A4	50C4	51A4	51B3	51C1	50B4	
14			50B4	50B3	51C2	51B1	51C3	51B1	51C3	51B1	51C2	50B3	49A1		
15					49A1	50A2	50A1	49A1	50A2	50A2	49A1				

Figure 7-4 Loading maps for Cycle 49 – benchmark cycle; fresh fuel, once-burned, and twice-burned fuel are denoted by the green, blue, and red colors

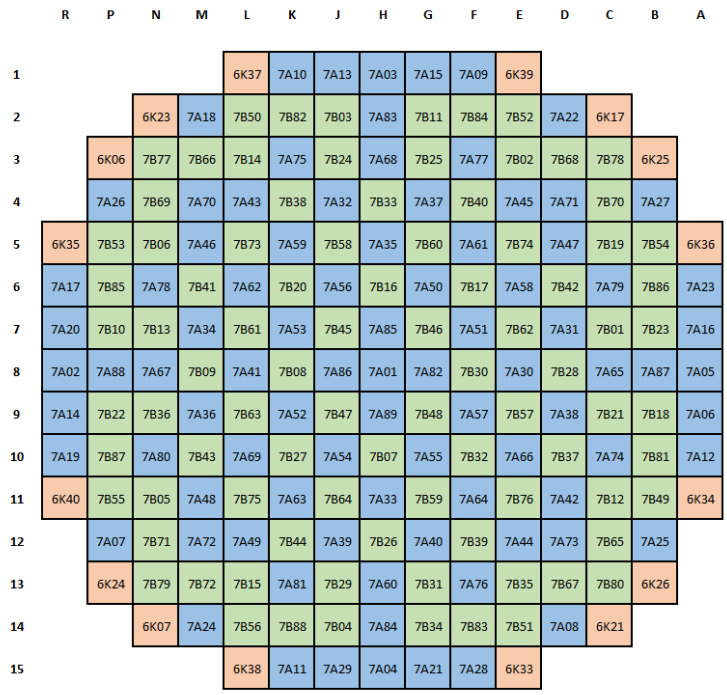

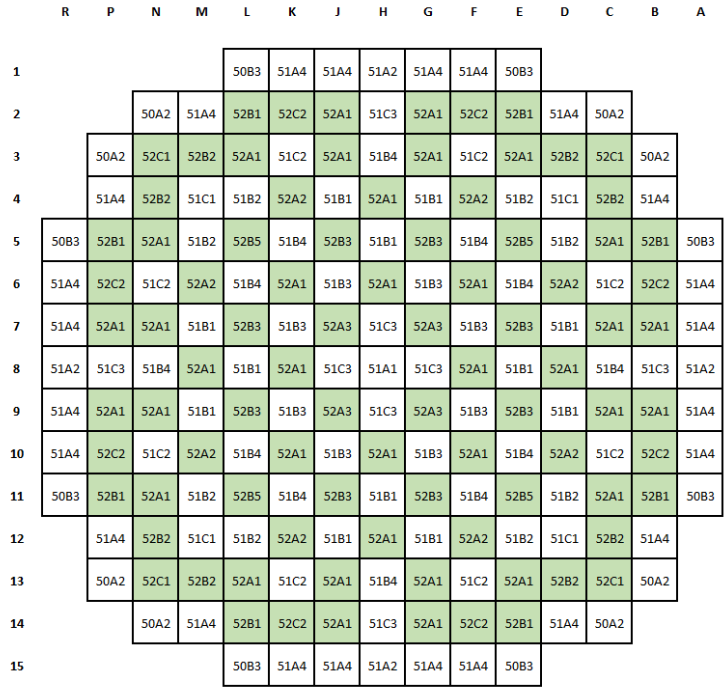

Figure 7-5 Loading maps for Cycle 50 – benchmark cycle; fresh fuel, once-burned, and twice-burned fuel are denoted by the green, blue, and red colors

7.3 Shuffling Scheme

The benchmark Cycle 48 was used as the cycle to perform equilibrium analysis of the full core on. In order to do so, this required intricate knowledge of the burnup maps and shuffling schemes as demonstrated in the figures and tables presented. The various information given in the form of assembly key tables, feed batch tables, and shuffling maps was used to recreate a computational model of the cycle in DYN3D. The primary goal of this analysis was to obtain results as close as possible for cycle length and discharge burnup of the specific core pertaining to those documented.

7.3.1 Convergence Approach

Converging on an equilibrium cycle is an iterative process that is complete once the discharge burnup of the current iteration is the same as that of the previous. While this is a mechanism that could be automated in future work, the number of iterations was deemed low enough such that this was not an imminent task.

DYN3D inputs involve an optional *brn* file, which gives the user the choice of specifying a spatial input distribution with respect to axial and radial nodes. In the first iteration of modeling the equilibrium core, an initial estimation of the spatial burnup distribution was inputted in the form of this file. Rather than start with a completely fresh core, three different guessed burnup distributions were assigned to individual assemblies based on whether they were fresh, once, or twice burned. Fresh assemblies were given an initial burnup vector of zeros, and once and twice burned assemblies were given cosine axial distributions as demonstrated in Figure 7-6.

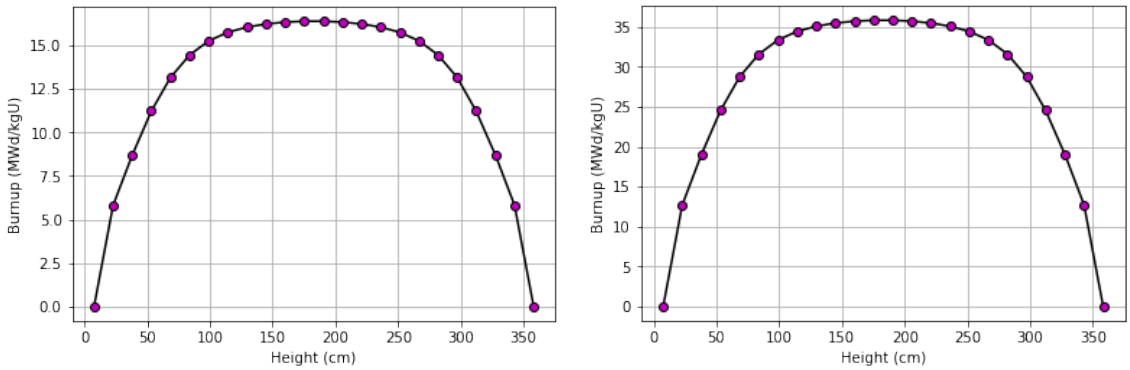

Figure 7-6 Axial input burnup distribution for (L) once-burned assemblies and (R) twice-burned assemblies

As well as the input burnup distribution file, DYN3D also provides an output burnup distribution file that gives burnup for every node at each time step. This file was used in conjunction with an interpolation scheme to obtain burnup distributions for each assembly at the current iteration's cycle length. These values were then used with the provided shuffling maps, as demonstrated below.

Figures 7-1 to 7-5 present the loading and shuffling maps given in the plant data document. As can be seen in Figure 7-7, the assembly keys were converted to indexed values, as were the burnup distribution outputs from the DYN3D *nbr* file. This allowed the shuffling to be done in a manner compliant with Python lists – the shuffling process was simplified to an indexing problem, and the shuffled *nbr* burnup values were converted to a new *brn* input file for the next iteration.

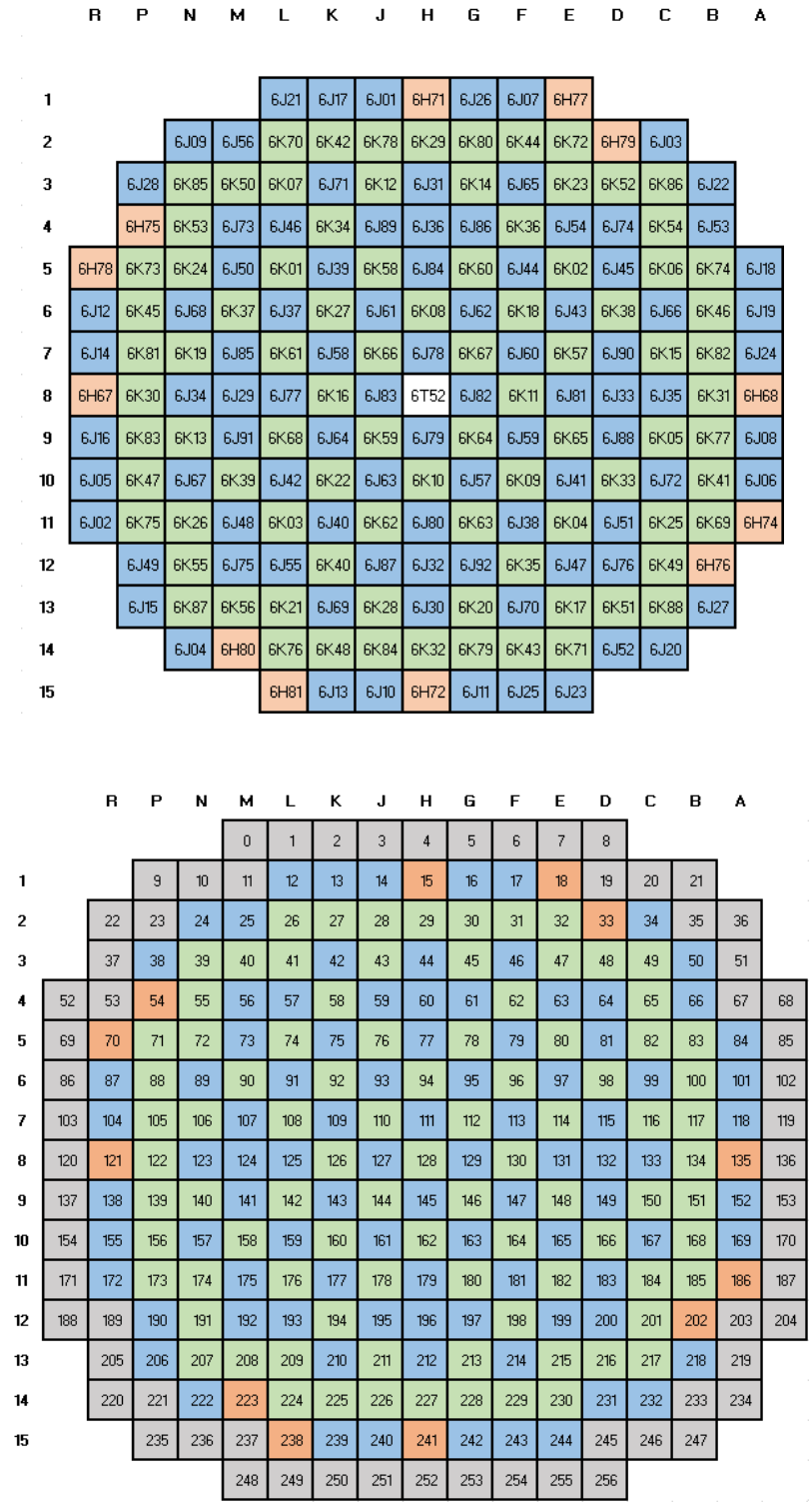

Figure 7-7 Given assembly keys and corresponding indexed full core model

Table 7-2 Shuffling keys from Cycle 47 to Cycle 48

	From	To		From	To		From	To
1	E3	L1	36	L7	J6	71	J14	C10
2	F6	K1	37	E7	G6	72	J13	A10
3	F8	J1	38	M10	E6	73	N5	R11
4	D14	H1	39	J2	C6	74	H14	M11
5	G13	G1	40	F10	A6	75	F4	K11
6	C9	F1	41	C7	R7	76	E2	H11
7	P13	E1	42	J7	M7	77	K4	F11
8	M8	N2	43	J5	K7	78	D13	D11
9	M13	M2	44	L2	H7	79	N2	A11
10	N14	D2	45	G5	F7	80	C12	P12
11	L3	C2	46	E5	D7	81	C13	M12
12	N11	P3	47	H10	A7	82	N12	L12
13	P9	K3	48	B4	R8	83	J9	J12
14	F14	H3	49	B6	N8	84	F2	H12
15	B9	F3	50	B10	M8	85	E11	G12
16	H4	B3	51	B11	L8	86	B8	E12
17	B13	P4	52	P11	J8	87	C13	D12
18	N3	M4	53	B5	G8	88	P3	B12
19	P8	L4	54	P5	E8	89	H12	P13
20	L5	J4	55	P6	D8	90	P7	K13
21	K14	H4	56	P10	C8	91	K2	H13
22	G7	G4	57	P12	A8	92	B7	F13
23	C4	E4	58	H6	R9	93	C5	B13
24	C3	D4	59	L11	M9	94	E13	N14
25	N4	B4	60	J11	K9	95	C2	M14
26	C14	R5	61	E14	H9	96	D3	D14
27	M3	M5	62	G11	F9	97	D8	C14

28	F12	K5	63	G9	D9	98	B3	L15
29	L14	H5	64	N9	A9	99	N7	K15
30	K12	H5	65	K6	R10	100	J3	J15
31	H2	D5	66	G14	N10	101	M2	H15
32	C11	A5	67	D6	L10	102	K8	G15
33	G3	R6	68	L9	J10	103	K10	F15
34	G2	N6	69	E9	G10	104	L13	E15
35	D10	L6	70	M6	E10			

Table 7-3 Equilibrium cycle convergence with respect to cycle length and burnup for Cycle 48

	Cycle Length (days)	Burnup (MWd/kgU)
Iteration 0	581.01346	25.8865
Iteration 1	436.51311	19.4482
Iteration 2	483.93777	21.2703
Iteration 3	455.68475	20.5526
Iteration 4	477.01672	20.8140

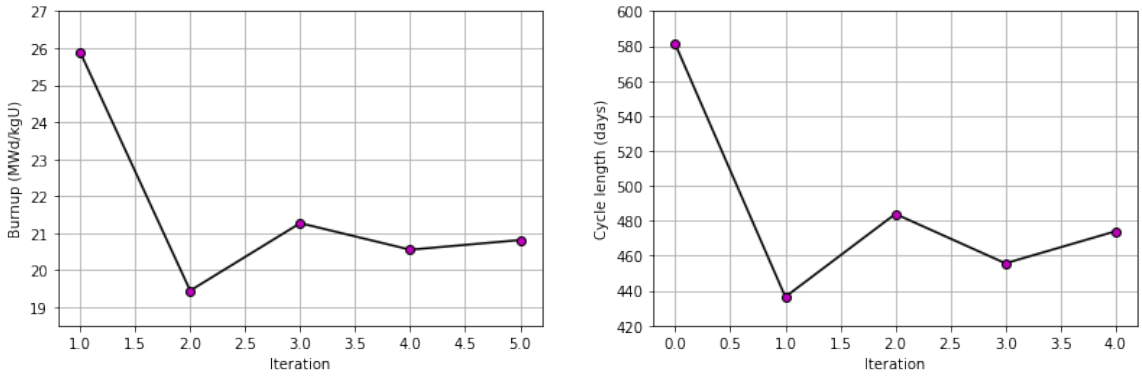

Figure 7-8 Convergence of (L) burn-up and (R) cycle length with equilibrium shuffling scheme

Table 7-4 Expected vs. calculated for discharge burnup and cycle length of equilibrium cycle

	Expected	Calculated	Error
B_d (MWd/kgU)	22.7604	20.814	8.55%
CL (days)	520	477.02	8.27%

Table 7-3 and Figure 7-8 demonstrate the convergence of Cycle 48 after 5 iterations, as the discharge burnup of the final iteration is within 1.2 percent of the previous stage. There is an error of around 8.55% in discharge burnup and around 8.266% for cycle length when compared to the data from the plant document – both discharge burnup and cycle length are lower than given in the reference data. The slight difference in error percentage can be attributed to the ways in which discharge burnup and cycle length were calculated. Cycle length was calculated assuming a linear curve at discharge and interpolating between the two points where the multiplication factor was equal to one, while discharge burnup was calculated using the outputs of the DYN3D files.

Once possible source of discrepancy in discharge burnup can possibly be attributed to the factor of an initial guess on the burnup distribution. Spectral effects can also account for up to 20-30 days. There were also guesses made on different assemblies, which will be discussed further in the missing information section of the concluding chapter.

The convergence cases demonstrate the reliance on the burnup distribution by oscillating between higher and lower numbers. If the previous case had a higher burnup distribution, then the next case is likely to have a longer cycle length as a result of a lower cycle length and less accumulated burnup.

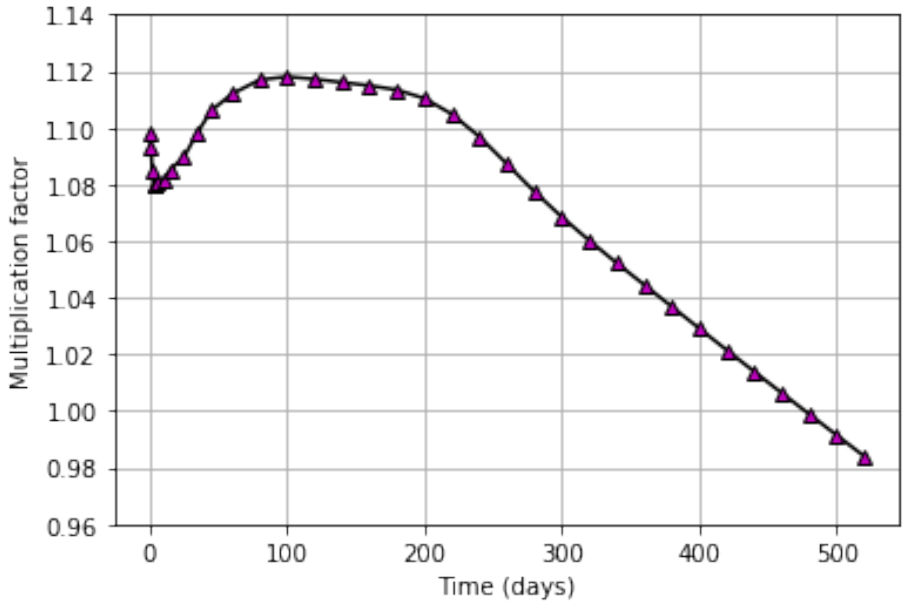

Figure 7-9 Core multiplication factor as a function of days

Figure 7-9 shows the core multiplication factor of the final equilibrium benchmarked cycle as a function of days. The plot demonstrates various points of interest within the life cycle of the core. First seen is the initial decrease in multiplication factor due to xenon poisoning, at which equilibrium is reached after around 8-10 days. Second is the effect of the burnable absorbers that cause in increase in multiplication factor until they are completely burned, at which point the multiplication factor begins its steady decline at around 100 days.

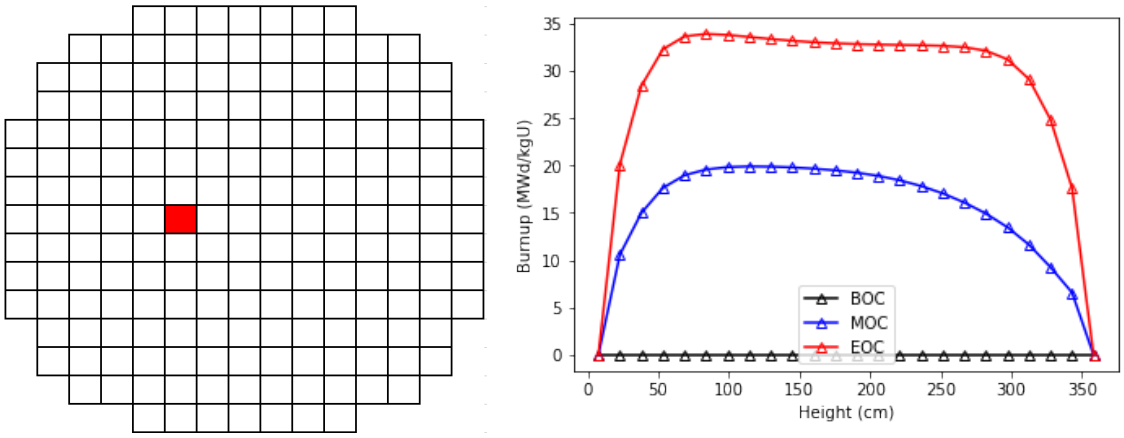

Figure 7-10 BOC, MOC, and EOC burnup as a function of axial height for an initially fresh fuel assembly near the center of the core

Figure 7-10 shows assembly burnup as a function of axial height for beginning, middle, and end of cycle for a fuel assembly close to the center of the core. The initial burnup distribution given was that of a fresh fuel assembly, and the plot demonstrates the accumulated burnup over the lifetime, which is typical.

Figures 7-11 and 7-12 show the same parameters but for fuel assemblies in different locations and with different initial burnup distributions. Figure 7-11 represents an initially once-burned assembly on the core periphery and Figure 7-12 represents and initially twice-burned assembly also on the core periphery. Both plots are in accordance with expected values of a 3-batch core.

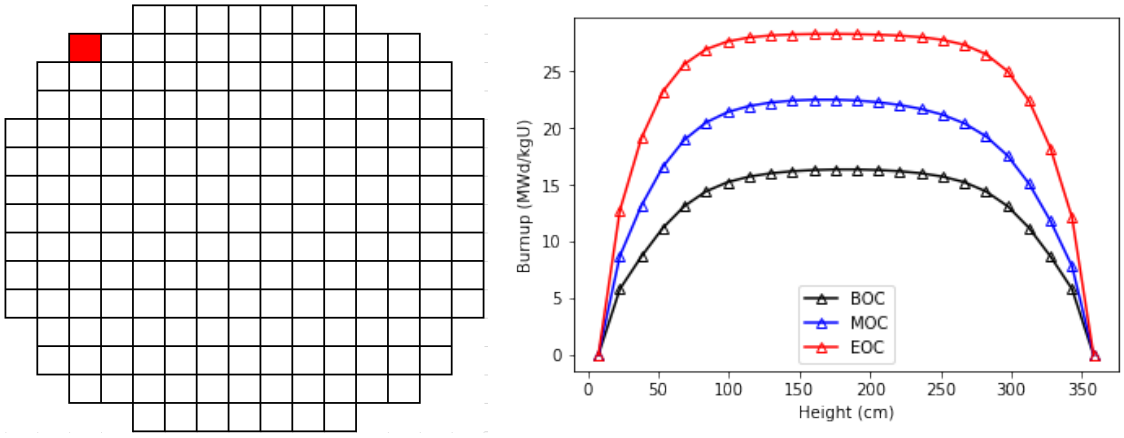

Figure 7-11 BOC, MOC, and EOC burnup as a function of axial height for an initially once-burned fuel assembly near the periphery of the core

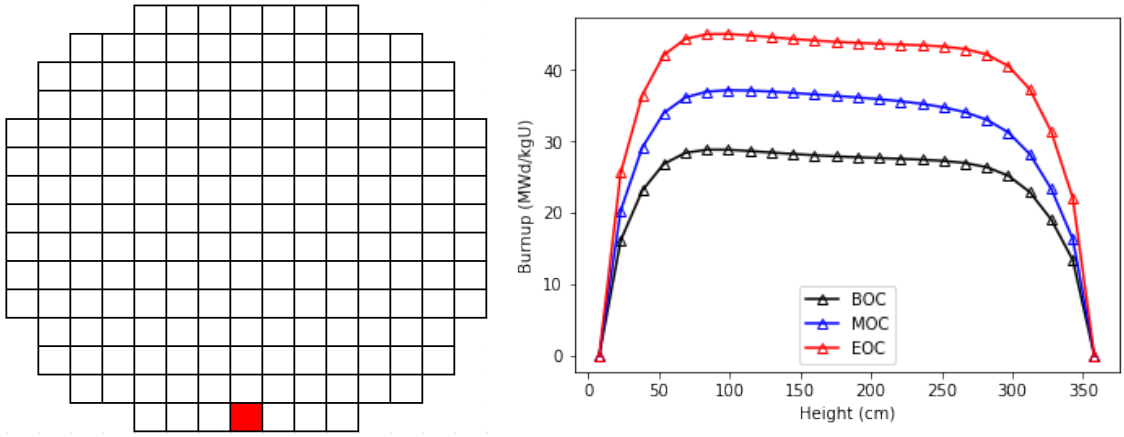

Figure 7-12 BOC, MOC, and EOC burnup as a function of axial height for an initially twice-burned fuel assembly near the periphery of the core

CHAPTER 8. CONCLUSIONS AND FUTURE WORK

This chapter presents a summary of the work performed in this thesis, missing information that could have contributed to discrepancies in certain results, and insight into possible future work that can be performed.

8.1 Conclusions

The primary outcome goal of this work was to develop and test a Monte Carlo-nodal diffusion code sequence that can be applied for modeling a new core with higher enriched fuel. This was done in various stages, as the required framework is extensive and consists of multiple variables in enrichment, loading patterns, and shuffling schemes.

The first step involved proving there exists potential for economic improvement by performing fuel cycle analysis on 2D assemblies. A theoretical enrichment was obtained for a 24-month cycle length, and its use in the fuel cycle was demonstrated to be economically viable, particularly when outage costs were factored in. The next overall goal was to confirm the utility of the two-step code sequence, but the compatibility between the codes had to first be verified. The analyses demonstrated very good agreement and reinforced the idea that generating 2D assembly cross-sections in Serpent was a reliable methodology for input into a full core model in DYN3D.

Finally, the output of the sequence was investigated with respect to known data. It did demonstrate some error, but this could be attributed to a number of variables and can surely be fine-tuned in future work. The purpose of the work was not to obtain perfect agreement, but to demonstrate that the sequence can achieve the goal of modeling a new cycle, in

which comparative results can be just as relevant as absolute ones. The overall results of the study indicate that it can be used for future work and could prove to be a valuable tool in modeling a higher enriched core with economic benefits and a longer cycle length.

8.2 Missing Data

Information provided to recreate the core was given in the form of materials, tables, and reload maps for the various cycles. However, there was some clarification necessary due to certain unknowns such as assembly key data from tables to maps. This section aims to describe this information and how it was accounted for.

8.2.1 Materials

Material data was given for enriched fuels, burnable absorbers, and clad. Fuel information relied on the ^{235}U enrichment and the assembly heavy metal loading. Therefore, density had to be back calculated using volume information as well. Please refer to the material Appendix for the full process of doing so. Burnable absorber information was provided in axial loading in both mg/cm and mg/in, so similar processes were used to calculate isotopic compositions for the input files. The process for doing so can also be seen in the material Appendix A.

8.2.1 Core Patterns and Fuel Management Data

For each cycle, three forms of assembly information were provided. First is a core loading table with assembly keys and corresponding values of enrichment, IFBA rods, WABA rods, and heavy metal loading for each unique assembly. Additional table contained feed batch, central zone, and fuel assembly IDs that match with adjacent reload maps. However, this is the only indication of which fuel assemblies are contained in the given loading maps. The remaining assembly locations had to be inferred. Documented below are the missing assemblies from Cycle 47, which are indicated in the loading patterns presented in Chapter 7 as 'XXXX' and tabulated below. These are of relevance to the equilibrium calculations of Cycle 48, as they serve as the once- and twice-burned assemblies in the core.

Table 8-1 Missing assembly locations and keys

Location	Key	Location	Key
R5	6G93	G1	6G94
R6	6G73	F1	6G63
R7	6G65	E1	6G92
R11	6G19	E15	6G27
L1	6G18	A5	6G21
L15	6G91	A9	6G67
K15	6G68	A10	6G62
J15	6G72	A11	6G90

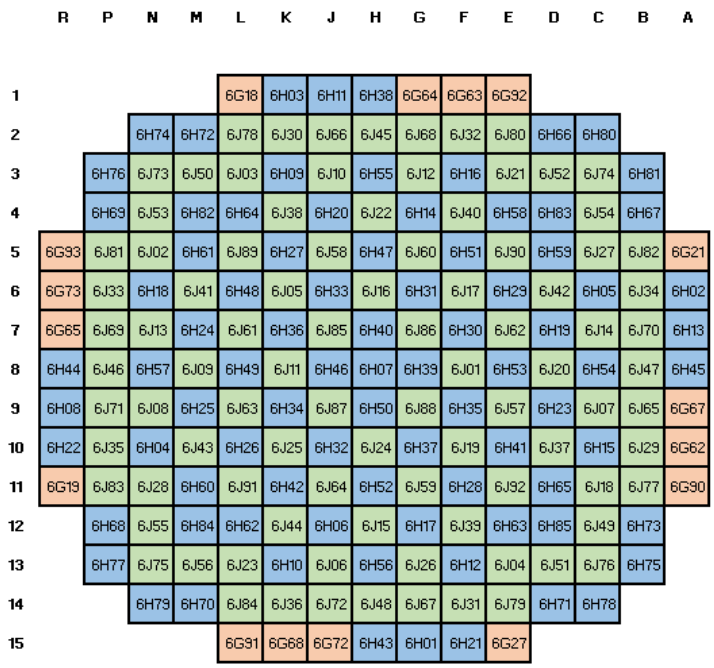

Figure 8-1 Cycle 47 core containing missing assemblies documented in Table 8-1

8.3 Future Work

While overall agreement between Serpent and DYN3D is good in general, there are a few ways to improve the modeling accuracy of the equilibrium cycle and plant data. Such methodology could include first accounting for spectral effects. Spectral history effects are the accumulation of errors in cross-sections due to the deviation of local operational conditions from average values. Since lattice codes assume average conditions for cross section generation, they cannot predict time and space dependencies that the fuel is subject to in a reactor core. There are various methodologies to account for these errors, such as micro-depletion, which calculates nuclide concentrations in each node and adds their contributions to the macroscopic absorption and fission cross sections [21]. This

methodology is worth exploring in future work, as it could notably improve the accuracy of the equilibrium cycle results.

Aside from fine tuning the agreement of the sequence with the plant data, the next step in this work would be to focus on creating a novel cycle involving a higher enriched core. As previously stated, the goal of this work was to establish a working sequence such that it could be applied to model such a core. While the agreement was important, the primary focus was to create the sequence that could be used to demonstrate the economic benefits of increasing the average core enrichment to higher values. The results of the 2D assembly analyses provide a starting point for an enrichment value that can now be investigated in such a model.

Future work will also include optimization of the various parameters of fuel enrichment, burnable absorber configurations, and enrichment of the burnable absorbers. Previous studies have not included factors such as varying loading patterns or optimization of burnable absorber rods, so these will definitely be included in further analyses. Finally, if the benefits can be demonstrated on a fully optimized 3D core model, the next stages would require overcoming licensing challenges and obtaining permits to allow commercial usage of such fuel.

APPENDICES

APPENDIX A: MATERIAL COMPOSITIONS

For the $\chi_{25} = 4.95\%$ enriched case the calculation would be done in the following manner. It is assumed that the enrichment of ^{234}U in the bundles is 0.8% of the ^{235}U enrichment.

$$\chi_{24} = 0.008 * 4.95\% = 0.0396\% \tag{A.1}$$

The rest of the heavy metal in the initial fuel loading is made up of ^{238}U calculated as

$$\chi_{28} = 100\% - 4.95\% + 0.0396\% = 95.0896\% \tag{A.2}$$

The atomic mass of uranium is calculated from these weight percents of uranium and the known isotopic masses:

$$M_U = \left[\frac{\chi_{24}}{M_{24}} + \frac{\chi_{25}}{M_{25}} + \frac{\chi_{28}}{M_{28}}\right]^{-1} = 237.8985268135428amu \tag{A.3}$$

The weight fractions of uranium and oxygen in uranium dioxide are determined by the following two expressions:

$$w_u = \frac{M_U}{M_U + 2 * M_O} = 0.881681882605617 \tag{A.4}$$

and

$$w_O = 1 - w_U = 0.118318117394383 \tag{A.5}$$

From the assembly dimensions and uranium heavy metal loading, the average density can be calculated. The total uranium heavy metal mass is $m_f = 482.386$ metric tons. The volume is calculated as

$$V_f = \pi * R_f^2 * H * N_{pins} \tag{A.6}$$

$$V_f = \pi * 0.392176^2 * 365.76 * 264 = 46656.486 cm^3 \tag{A.7}$$

The fuel density is calculated by computing the uranium heavy metal density and dividing by its fractional weight

$$\rho_f = \frac{m_f}{V_f * w_U} = 10.339098312689 \frac{g}{cm^3} \tag{A.8}$$

Concentration of the WABA material was provided in units of axial loading, both mg/in and mg/cm. The atomic density is b/cm is calculated both for ^{10}B and C as

$$N(B10) = \frac{(WABA\ axial\ loading \div 1000) * N_{av}}{(Area\ of\ WABA\ material) * (B10\ molar\ mass)} = \frac{(6.03 \div 1000) * 0.6022}{0.1276 * 10.0129} = 0.0028 \tag{A.9}$$

Since the poison material is B_4C, then the number of carbon atoms NC is N(B10)/4, or 7.1079E-04. The WABA material is an alloy of Al_2O_3-B_4C, so the concentrations of Al and O are calculated as

$$N(Al_2O_3) = \frac{(wf\ of\ Al\ in\ mix) * \left(\rho_{Al_2O_3}\right) * (Al_2O_3\ porosity) * (N_{av})}{Al_2O_3\ atomic\ weight}$$
$$= \frac{0.86 * 3.95 * 0.95 * 0.602214086}{2 * 26.98154 + 3 * 15.9999} = 0.0191 \quad \text{(A.10)}$$

Thus, the compositions of Al and O are given by $N(Al) = 2 * N(Al_2O_3) = 0.0381$ and $N(O) = 3 * N(Al_2O_3) = 0.0572$.

The IFBA coating concentration is calculated in a similar manner to the WABA material,

$$N(B10) = \frac{(IFBA\ axial\ loading \div 1000) * N_{av}}{(Area\ of\ IFBA\ material) * (B10\ molar\ mass)}$$
$$= \frac{(0.8858 \div 1000)}{0.0025 * 10.0129} = 0.0216 \quad \text{(A.11)}$$

Since the poison material is ZrB_2 then $N(Zr) = N(B10) \div 2 = 0.0108$.

REFERENCES

[1] S. Michael, "Plant Data Transfer. For Georgia Tech Nuclear Engineering Core Design Studies and Benchmarking," Framatome Inc., Rep. FSI-0043332 Rev. 1, Jun. 2019.

[2] J. Leppänen, M. Pusa, T. Viitanen, V. Valtavirta, and T. Kaltiaisenaho, "The serpent monte carlo code: Status, development and applications in 2013.," *Annals of Nuclear Energy,* vol. 82, pp. 142-15, 2015.

[3] E. Fridman and J. Leppänen, "On the use of the serpent monte carlo code for few-group cross section generation.," *Annals of Nuclear Energy,* vol. 38, pp. 1399-1405, 2011.

[4] J Leppänen, "On the use of delta-tracking and the collision flux estimator in the serpent 2 monte carlo particle transport code.," *Annals of Nuclear Energy,* vol. 105, pp. 161-167, 2017.

[5] R. Ulrich, K. Kliem, U. Grundman, S. Baier, Y. Bilodid, S. Duerigen, and E. Fridman, "The reactor dynamics code dyn3d – models, validation, and applications," *Progress in Nuclear Energy,* 2016.

[6] Y. Bilodid, E. Fridman, D. Kotlyar, and E. Shwagerus, "Explicit decay heat calculation in the nodal diffusion code dyn3d.," *Annals of Nuclear Energy,* vol. 121, pp. 382-389, 2018.

[7] E. Nikitin and E. Fridman, "Extension of the reactor dynamics code dyn3d to sfr applications – part i: Thermal expansion models.," *Annals of Nuclear Energy,* vol. 118, pp. 382-389, 2018.

[8] A. Johnson, D. Kotlyar, G. Ridley, S. Terlizzi, and P. Romano, "Core-gatech-group/serpent-toools: 0.5.2a1 – pre-release.," *Annals of Nuclear Energy,* 2018.

[9] U.S. Nuclear Regulatory Commission, "Criticality Accident Requirements," NRC Library, 50.68 (2017).

[10] Nuclear Energy Institute, "The Economic Benefits and Challenges with Utilizing Increased Enrichment and Fuel Burnup for Light-Water Reactors," NEI White Paper (2019).

[11] M. J. DRISCOLL, T. J. DOWNAR and E. E. PILAT, The Linear Reactivity Model for Nuclear Fuel Management, American Nuclear Society, LaGrange Park, Illinois (1990).

[12] E. Fridman, S. Kliem. "Pu recycling in a full Th-MOX PWR core. Part I: Steady state analysis," *Nuclear Engineering and Design* 241, 193-202 (2011).

[13] Electric Power Research Institute, "PWR Primary Water Chemistry Guidelines: Revision 2," EPRI TR-107728-V2, vol. 2 (1997).

[14] The Ux Consulting Company, LLC, 2019. https://www.uxc.com/p/prices/UxCPrices.aspx.

[15] J. Duderstadt and L. Hamilton, *Nuclear Reactor Analysis*. Wiley, 1976.

[16] J. R. Lamarsh and A. J. Baratta, *Introduction to Nuclear Engineering*, vol. 23, no. 1. 1955.

[17] U. Rohde et al., "The reactor dynamics code DYN3D - Models, validation and applications," *Prog. Nucl. Energy*, vol. 89, pp. 170–190, 2016.

[18] D. A. Brown et al., "ENDF/B-VIII.0: The 8thMajor Release of the Nuclear Reaction Data Library with CIELO-project Cross Sections, New Standards and Thermal Scattering Data," *Nucl. Data Sheets*, vol. 148, pp. 1–142, 2018.

[19] Y. Bilodid, D. Kotlyar, E. Shwageraus, E. Fridman, and S. Kliem, "Hybrid microscopic depletion model in nodal code DYN3D," *Ann. Nucl. Energy*, vol. 92, pp. 397–406, 2016.

[20] K. Smith, "Assembly Homogenization Techniques for Light Water Reactor Analysis," *Progress in Nuclear Energy*, vol. 17, pp. 303–335, 1986.

[21] A. Bernal, J.E. Roman, R. Miro, and G. Verdu, "Assembly Discontinuity Factors for the Neutron Diffusion Equation discretized with the Finite Volume Method. Application to BWR," *Ann. Nucl. Energy*, vol. 97, pp. 76–85, 2016.

[22] C. Yi and G. Sjoden, "Energy group structure determination using particle swarm optimization," *Annals of Nuclear Energy*, vol. 56, pp. 53-56 (2013).

[23] A. Yamamoto and K. Kanda, "Comparison between Equilibrium Cycle and Successive Multicycle Optimization Methods for In-Core Fuel Management of Pressurized Water Reactors," *Journal of Nuclear Science and Technology*, vol. 34, pp. 882-892 (1997).

[24] Yaqi Wang, Sebastian Schunert, and Vincent Laboure. *Rattlesnake Theory Manual*. INL. 2017.

[25] F. Rahnema, D. Zhang, "Continuous energy coarse mesh transport (COMET) method," *Annals of Nuclear Energy,* vol. 115, pp. 601-610 (2018).

[26] W. Daniel, "Modeling Integral Fuel Burnable Absorbers Using the Method of Characteristics," Master's Thesis, University of Tennessee, 2014.

[27] S. Stimpson, B. Collins, A. Godfrey, F. Franceschini, D. Salazar, "Extended Radial Reflector Modeling Capabilities in IMPACT," *International Conference on Mathematics & Computational Models Applied to Nuclear Science and Engineering,* 2017.